RESEARCH ARTICLE | JULY 08 2025

How does the limited resolution of space plasma analyzers affect the accuracy of space plasma measurements?

G. Nicolaou ■ (a) ; C. Ioannou (b) ; C. J. Owen (b) ; D. Verscharen (b) ; A. Fedorov (c) ; P. Louarn (c)



Rev. Sci. Instrum. 96, 075203 (2025) https://doi.org/10.1063/5.0218667





Articles You May Be Interested In

Two-scale structure of the current layer controlled by meandering motion during steady-state collisionless driven reconnection

Phys. Plasmas (July 2004)





09 July 2025 07:16:42

How does the limited resolution of space plasma analyzers affect the accuracy of space plasma measurements?

Cite as: Rev. Sci. Instrum. 96, 075203 (2025); doi: 10.1063/5.0218667

Submitted: 13 May 2024 • Accepted: 2 June 2025 •

Published Online: 8 July 2025























AFFILIATIONS

- Department of Space and Climate Physics, Mullard Space Science Laboratory, University College London, Dorking, Surrey RH5 6NT, United Kingdom
- ²Institut de Recherche en Astrophysique et Planétologie, 9, Avenue du Colonel Roche, BP 4346, 31028 Toulouse Cedex 4, France
- a) Author to whom correspondence should be addressed: g.nicolaou@ucl.ac.uk

ABSTRACT

We investigate the systematic errors in measured plasma velocity distribution functions and their corresponding velocity moments, arising from the limited energy and angular resolution of top-hat electrostatic analyzers. For this purpose, we develop a forward model of a concept analyzer that simulates observations of typical solar wind proton plasma particles with their velocities following a Maxwell distribution function. We then review the standard conversion of the observations to physical parameters and evaluate the errors arising from the limited resolution of the modeled instrument. We show that the limited resolution of the instrument results in velocity distributions that underestimate the core and overestimate the tails of the actual Maxwellian plasma velocity distribution functions. As a consequence, the velocity moments of the observed plasma underestimate the proton density and overestimate the proton temperature. Moreover, we show that the examined errors become significant for cold and fast plasma protons. We finally determine a mathematical formula that predicts these systematic inaccuracies based on specific plasma inputs and instrument features. Our results inform and contextualize future evaluations of observations by analyzers in various plasma regimes.

© 2025 Author(s). All article content, except where otherwise noted, is licensed under a Creative Commons Attribution (CC BY) license (https://creativecommons.org/licenses/by/4.0/). https://doi.org/10.1063/5.0218667

I. INTRODUCTION

Top-hat electrostatic analyzers (ESAs) with aperture deflectors and position-sensitive detectors measure the number of incoming charged plasma particles in discrete energy-per-charge, elevation, and azimuth bins. 1-7 With these measurements, we can construct the three-dimensional (3D) velocity distribution functions (VDFs) of the plasma species measured by the instrument. However, plasma measurements are subject to several errors, which propagate inaccuracies to the determined VDFs and determined data products, such as the density, bulk speed, and temperature of the detected

For instance, similar to any other counting experiment, the number of detected particles has a statistical uncertainty governed by Poisson statistics. This uncertainty propagates statistical errors to the physical parameters that we determine from the observations. 8-10 Moreover, the statistical uncertainties of the observations lead to systematic uncertainties in the plasma parameters if the typical chi-squared minimization method is used to infer the underlying plasma VDFs. 11-13 Such systematic errors may lead to artificial correlations between the plasma parameters, which is not only preventing the resolution of physical mechanisms in space but also may alter the outcome of scientific studies, leading to erroneous conclusions.14

Plasma particle observations are subject to background noise caused by the instrument electronics. The analysis of the VDFs constructed from the noisy observations leads to an overestimation of the zeroth- and second-order velocity moments, which determine the plasma density and temperature, respectively. 15,16 Moreover, the background noise affects the determination of particle distribution functions, even when determined by the chi-squared minimization technique.¹⁷ Therefore, the noise should either be monitored

on-board⁵ or estimated by on-ground analyses ^{16,18,19} and subtracted from observations prior any further analysis.

Other studies have also evaluated the systematic uncertainties in the plasma parameters resulting from non-resolved time variations of the plasma. ^{20,21} Plasma bulk velocity fluctuations on time scales below the time-resolution of plasma instruments are expected to result in a broadening of the resolved plasma VDFs and thus, in an overestimation of the plasma temperature. If the velocity fluctuations are more dominant in either the perpendicular or the parallel direction with respect to the background magnetic field, the analysis of the observations may determine false temperature anisotropies. ²⁰

We also expect systematic uncertainties in the recovered VDFs if the instrument is not capable of resolving VDFs of different species. For instance, solar wind proton VDFs may have significant energy overlap with the VDFs of α particles. In these cases, the analysis may fail to examine the VDFs of the two species separately

and return false results. ^{10,22} More specifically, if the alpha particles are treated as protons, the analysis overestimates the actual proton density, speed, and temperature. ²³

In addition to the errors mentioned above, we expect additional systematic errors in the plasma interpretations due to the limited angular and energy resolution of ESAs. ESAs sample the plasma particles in discrete energy-per-charge and angular bins, with each bin covering a finite volume in velocity space. The measurements, however, cannot resolve the shape of the VDFs within each bin. Although such systematic errors have been discussed in previous publications, ^{24,25} we argue that since there is a significant number of studies using plasma observations by ESAs, there is a need for a dedicated study to provide a detailed methodology to evaluate and estimate them.

In Sec. II, we explain the motivation for this study in detail. Section III shows the methodology that we follow to simulate plasma

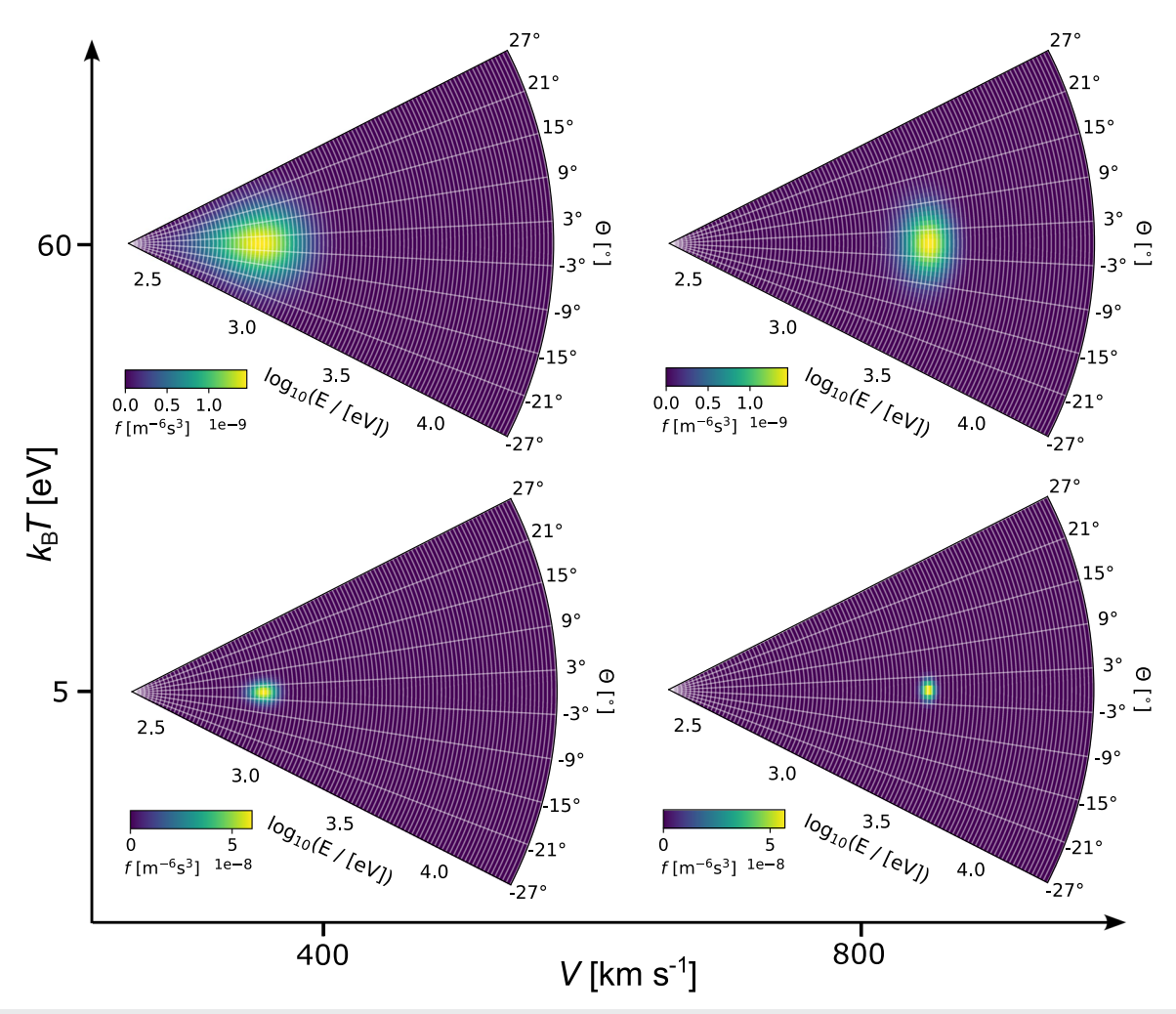


FIG. 1. Energy (velocity) distribution function models for different plasma bulk speeds and temperatures. Each panel shows a modeled distribution as a function of particle energy and elevation for the azimuth direction of the bulk velocity. The white grid on each panel represents the energy and elevation bins that are similar to those of our concept instrument (see Sec. III A).

observations and how we construct the velocity distributions of the plasma. We further explain how we quantify the systematic errors by comparing the constructed distributions and their velocity moments with their respective simulated plasma distributions and their moments. In Sec. IV, we present our results considering a wide range of plasma proton properties. In Sec. V, we discuss our results in detail, including the potential impact of the demonstrated uncertainties to scientific studies. We also compare the systematic errors to an analytical function to predict the systematic uncertainties as functions of the plasma VDF derivatives and the instrument resolution. Finally, we discuss a potential mitigation strategy.

II. MOTIVATION

Due to their finite angular and energy resolution, plasma analyzers cannot provide any information about the "shape" of the plasma distribution function within each energy-per-charge and angular bin. Instead, analyzers return one value (number of counts) per bin, which we usually consider as representative of the value of the distribution function at the central energy-per-charge, elevation, and azimuth of the corresponding bin. Analyses of these observations then determine the physical parameters of the plasma. Such simplifications which neglect the details of the instrument response and the shape of the plasma velocity distribution on small, sub-bin scales may be valid in numerous cases. Here, however, we argue that it is not always safe to adopt them. In Fig. 1, we show modeled Maxwellian energy distribution functions of protons for four different combinations of plasma bulk speeds and temperatures. All four distributions have a bulk velocity vector along elevation angle $\Theta = 0^{\circ}$ and azimuth angle $\Phi = 0^{\circ}$, and we show two-dimensional 2D "cuts" of the distribution at azimuth $\Phi = 0^{\circ}$, as functions of particle energy E and elevation Θ (see Sec. III for details). The white grid on each panel shows energy-elevation bins with size $\delta E/E \times \delta \Theta$ $\approx 0.05 \times 6^{\circ}$. The gradients of the distribution over individual instrument bins become significant as the bulk speed increases and the plasma temperature decreases. Thus, under certain plasma conditions, simplifying the analysis by assuming that the distribution does not vary significantly within each bin can be inappropriate. This study investigates the accuracy of this simplification when applied to standard solar wind proton plasma measurements by an electrostatic analyzer concept and demonstrates the methodology for carrying

out accuracy tests. Although this study is carried out using a specific instrument model, the demonstrated methodology can be used for any similar instrument after the proper adjustment of the model.

III. METHODOLOGY

A. Concept instrument

We model the response of a typical top-hat electrostatic analyzer for solar wind proton measurements. A diagram of this design is shown in Fig. 2. In one full acquisition, our concept instrument measures the number of particles in 96 energy-per-charge bins, E/q, nine elevation bins, Θ , and 11 azimuth sectors, Φ . The elevation angle is determined as the angle between the velocity vector of the incoming particles and the top-hat plane, while the azimuth angle is the angle between the projection of the particle velocity vector on the top-hat plane (same as the detection plane) and a reference axis onto that plane (see Fig. 2). Since we simulate protons (charge q = 1), we refer to E/q steps as energy steps E throughout this paper. The 96 E steps are exponentially spaced over a range spanning from 200 eV to 20 keV. The nine Θ bins sample particles with elevation angles from -24° to $+24^{\circ}$, while the 11 Φ sectors cover azimuth directions from -32° to $+32^{\circ}$. The elevation and azimuth bins are equally spaced across their corresponding sampling range of angles. The values of E, Θ , and Φ bins we report above correspond to the energies, elevations, and azimuths sampled in the center of each bin.

B. Input velocity distribution functions

In order to simulate observations of our concept instrument, we first setup a velocity distribution function of the "measured" plasma particles. We consider solar wind protons, with their velocities following the 3D isotropic Maxwellian distribution function,

$$f(\vec{V}) = N_{\rm in} \left(\frac{m}{2\pi k_{\rm B} T_{\rm in}}\right)^{\frac{3}{2}} e^{-\frac{m(\vec{V} - \vec{V}_{\rm in})^2}{2k_{\rm B} T_{\rm in}}},\tag{1}$$

where m is the proton mass; $k_{\rm B}$ is the Boltzmann constant; \vec{V} is the individual proton particle velocity; and $N_{\rm in}$, $T_{\rm in}$, and $\vec{V}_{\rm in}$ are the proton plasma density, temperature, and bulk velocity, respectively. Since electrostatic analyzers resolve particle distributions in a spherical reference frame, we express $f(\vec{V})$ in terms of the individual

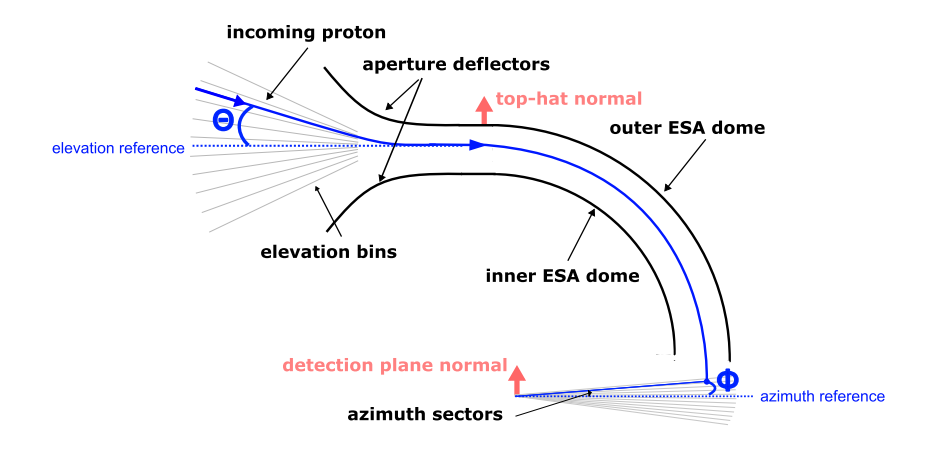


FIG. 2. Schematic of our concept instrument. We consider a typical top-hat electrostatic analyzer with aperture deflectors and a position-sensitive detector, which can resolve energies, elevation, and azimuth directions of solar wind protons.

particle energy $\varepsilon = \frac{1}{2}m\vec{V}\cdot\vec{V}$, elevation θ , and azimuth ϕ directions as

$$f(\varepsilon,\theta,\phi) = N_{\rm in} \left(\frac{m}{2\pi k_{\rm B} T_{\rm in}}\right)^{\frac{3}{2}} e^{-\frac{\varepsilon + \varepsilon_0 - 2\sqrt{\varepsilon c_0} \cos \omega(\theta,\phi)}{k_{\rm B} T_{\rm in}}},$$
 (2)

where $\varepsilon_0 = \frac{1}{2} m \vec{V}_{in} \cdot \vec{V}_{in}$ is the bulk energy of the plasma particles and $\omega(\theta,\phi)$ is the angle between the individual particle velocity vector \vec{V} and the bulk velocity vector \vec{V}_{in} . ^{22,26,27}

C. Forward modeling

In each acquisition, the instrument records the number of particles in discrete E, Θ , and Φ bins. The expected number of counts (recorded number of particles) in each E, Θ , Φ bin for a single acquisition is 21,28

$$C_{\exp}(E, \Theta, \Phi) = \Delta \tau \int_{\varepsilon_{\min}}^{\varepsilon_{\max}} \int_{\theta_{\min}}^{\theta_{\max}} \int_{\phi_{\min}}^{\phi_{\max}} \alpha(E, \Theta, \Phi, \varepsilon, \theta, \phi)$$

$$\times f(\varepsilon, \theta, \phi) \frac{2}{m^{2}} \varepsilon d\varepsilon \cos \theta d\theta d\phi, \qquad (3)$$

where $\Delta \tau$ is the duration of each acquisition and $\alpha(E,\Theta,\Phi,\varepsilon,\theta,\phi)$ is the effective aperture area, which, in general, varies with the sampled energy and direction. The limits of the integral are determined by the minimum and maximum energy, elevation, and azimuth angle of the particles that can be detected in each bin. We now assume that for our concept instrument,

$$\alpha(E,\Theta,\Phi,\varepsilon,\theta,\phi)\cos\theta = \alpha_0 \exp\left[-\frac{\left(\frac{\varepsilon}{E} - 1 + \frac{\theta - \Theta}{S_{E\Theta}}\right)^2}{2\left(\frac{\sigma_E}{E}\right)^2}\right] \times \exp\left[-\frac{(\theta - \Theta)^2}{2(\sigma_{\Theta})^2}\right] \exp\left[-\frac{(\phi - \Phi)^2}{2(\sigma_{\Theta})^2}\right],$$
(4)

where we consider the same α_0 for each E,Θ,Φ bin. For this study, we adjust α_0 , such that the peak of $C_{\exp}(E,\Theta,\Phi)$ is 10 000 counts for each sample that we simulate. The standard deviations σ_E , σ_Θ , and σ_Φ describe the width of the transmission curves along ε , θ , and ϕ , respectively, within each E,Θ,Φ bin. Our concept instrument has $\sigma_E \sim 0.02E, \ \sigma_\Theta \sim 2.55^\circ$, and $\sigma_\Phi \sim 2.72^\circ$. Equation (4) implies that the energy of the peak of the transmission depends on the elevation angle, which is a standard feature of electrostatic analyzers. This energy-elevation coupling of the response is adjusted by the $S_{E\Theta}$ term, which in our model is set to $S_{E\Theta} = 120$, which simulates a response that is similar to the electron plasma spectrometer (CAPS/ELS) on Cassini^{1,30} and the Solar Wind Around Pluto (SWAP) on New Horizons. $^{10.29}$ Figure 3(a) shows $\alpha\cos\theta/\alpha_0$ of our model instrument as a function of $\frac{\varepsilon}{E}$ and θ , for $\phi = \Phi$. Figure 3(b) shows $\alpha\cos\theta/\alpha_0$ as a function of $\frac{\varepsilon}{E}$ and ϕ , for $\theta = \Theta$, and Fig. 3(c) shows $\alpha\cos\theta/\alpha_0$ as a function of θ and ϕ , for ε in Eq. (2).

We simulate the expected number of counts in each E, Θ, Φ bin based on Eq. (3) and using the expressions for the effective aperture and response function as explained above. To solve the triple integral numerically, we substitute the integrals with sums, i.e.,

$$C_{\exp}(E,\Theta,\Phi) = \Delta \tau \sum_{i=1}^{25} \sum_{j=1}^{25} \sum_{k=1}^{25} \alpha_0 \exp \left[-\frac{\left(\frac{\varepsilon_i}{E} - 1 + \frac{\theta_j - \Theta}{S_{E\Theta}}\right)^2}{2\left(\frac{\sigma_E}{E}\right)^2} \right] \times \exp \left[-\frac{\left(\theta_j - \Theta\right)^2}{2\left(\sigma_\Theta\right)^2} \right] \exp \left[-\frac{\left(\phi_k - \Phi\right)^2}{2\left(\sigma_\Phi\right)^2} \right] \times f(\varepsilon_i,\theta_j,\phi_k) \frac{2}{m^2} \varepsilon_i \, d\varepsilon_i \, d\theta_j \, d\phi_k, \tag{5}$$

where we divide the acceptance width of each bin in discrete steps ε_i , θ_j , ϕ_k . Appendix A shows how we optimize our model and decide to use $25 \times 25 \times 25$ of $\varepsilon_i \times \theta_j \times \phi_k$ steps. In each bin, we assign a measurement $C(E, \Theta, \Phi)$, which is taken randomly from the Poisson distribution with expectation value $C_{\text{exp}}(E, \Theta, \Phi)$. This is done to

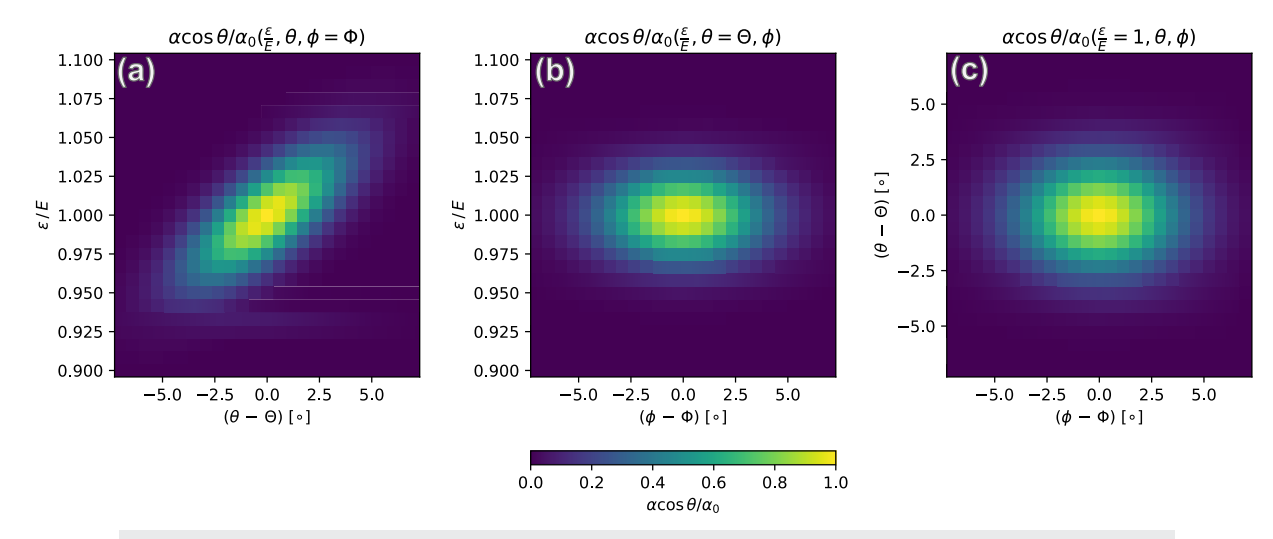


FIG. 3. $\alpha\cos\theta/\alpha_0$ of our instrument model as a function of (a) $\frac{\varepsilon}{\varepsilon}$ and θ , for $\phi=\Phi$, (b) $\frac{\varepsilon}{\varepsilon}$ and ϕ , for $\theta=\Theta$, and (c) θ and ϕ , for $\frac{\varepsilon}{\varepsilon}=1$.

model the statistical uncertainty of each measurement. $^{13-15,31,32}$ Nevertheless, the adjustment of α_0 , as explained above, reduces biases caused by statistical errors.

D. Plasma distributions constructed from observations

To construct the 3D VDFs from *in situ* observations, we treat the particle energy ε , elevation θ , and azimuth ϕ as constants over the acceptance width of each bin and equal to their central values E, Θ , and Φ , respectively. Thus, the distribution function is $f(E, \Theta, \Phi)$, and also constant within the acceptance width of each E, Θ, Φ bin. With this approximation, Eq. (3) becomes

$$C_{\exp}(E,\Theta,\Phi) \sim f(E,\Theta,\Phi) \frac{2}{m^2} \Delta \tau E^2 \int_{\varepsilon_{\min}}^{\varepsilon_{\max}} \int_{\phi_{\min}}^{\phi_{\max}} \int_{\phi_{\min}}^{\phi_{\max}} \times \alpha(E,\Theta,\Phi,\varepsilon,\theta,\phi) \frac{d\varepsilon}{E} \cos\theta \,d\theta \,d\phi, \tag{6}$$

where the integral on the right-hand side term is the energydependent, effective geometric factor of the instrument,

$$G(E,\Theta,\Phi) \equiv \int_{\varepsilon_{\min}}^{\varepsilon_{\max}} \int_{\theta_{\min}}^{\theta_{\max}} \int_{\phi_{\min}}^{\phi_{\max}} \alpha(E,\Theta,\Phi,\varepsilon,\theta,\phi) \frac{d\varepsilon}{E} \cos\theta \,d\theta \,d\phi. \quad (7)$$

Under this simplification then,^{31–33} the expected number of counts in each bin is

$$C_{\exp}(E,\Theta,\Phi) \sim \frac{2}{m^2} G(E,\Theta,\Phi) E^2 f(E,\Theta,\Phi) \Delta \tau.$$
 (8)

Assuming further that the obtained measurements $C(E, \Theta, \Phi)$ are representative of the expected counts, then it is straightforward to convert the observations to plasma distribution functions using

$$f_{\text{out}}(E,\Theta,\Phi) \sim \frac{m^2}{2G(E,\Theta,\Phi)E^2\Delta\tau}C(E,\Theta,\Phi).$$
 (9)

Equation (9) fails to describe plasma measurements when the underlying distribution functions change significantly over the acceptance width of each bin of the instrument. In this study, we investigate the accuracy of the approach used in Eq. (9). In order to do that, we simulate observations $C(E, \Theta, \Phi)$ using a high-resolution model as described in Sec. III C and in Appendix A, for Maxwellian proton distribution functions for a range of input bulk speeds $V_{\rm in}$ and temperatures $T_{\rm in}$. We then compare the differences between the constructed $f_{\rm out}(E, \Theta, \Phi)$ and the input distributions $f(E, \Theta, \Phi)$ and the differences between their velocity moments, as we explain in Sec. III E.

E. Quantifying the inaccuracies

Our evaluation is based on the comparison between the input distribution functions $f(E,\Theta,\Phi)$ and the corresponding distributions that we construct from the simulated observations $f_{\text{out}}(E,\Theta,\Phi)$. For different sets of input parameters, we calculate the distribution of the residuals,

$$F_{\rm residual}(E,\Theta,\Phi) = \log_{10}[f_{\rm out}(E,\Theta,\Phi)] - \log_{10}[f(E,\Theta,\Phi)], \quad (10)$$

considering only E, Θ, Φ bins with $C(E, \Theta, \Phi) > 1$. For each combination of the input plasma parameters, we calculate the mean absolute value of the residuals as

$$R = \frac{1}{N_{\rm E} \times N_{\Theta} \times N_{\Phi}} \sum_{i=1}^{N_{\rm E}} \sum_{j=1}^{N_{\rm \Theta}} \sum_{k=1}^{N_{\rm \Phi}} |F_{\rm residual}(E_i, \Theta_j, \Phi_k)|, \qquad (11)$$

where indices i,j,k now indicate the individual energy, elevation, and azimuth bins, respectively, of the instrument with $C(E,\Theta,\Phi)>1$. Finally, in order to estimate the impact of the limited instrument resolution on the plasma bulk parameters, for each set of input plasma parameters, we compare the velocity moments of $f_{\text{out}}(E,\Theta,\Phi)$ and the corresponding velocity moments of $f(E,\Theta,\Phi)$. We calculate the first three orders of velocity moments of each f_{out} and f, determining the corresponding densities N_{out} and N_f , speeds V_{out} and V_f , and temperatures T_{out} and T_f (see Appendix B). Although $f(E,\Theta,\Phi)$ is the value of the input distribution at the center of each E,Θ,Φ bin, we do not expect the determined moments N_f , V_f , and T_f to be identical to their corresponding input parameters N_{in} , V_{in} , and T_{in} , due to the limited sampling of the distribution. However, we expect that N_f , V_f , and T_f would be identical to the corresponding moments of f_{out} for cases with negligible error. Thus, for the purposes of this study, we investigate the ratios $\frac{N_{\text{out}}}{N_f}$, $\frac{V_{\text{out}}}{V_f}$, and $\frac{T_{\text{out}}}{T_f}$.

IV. RESULTS

Figure 4(a) shows a 2D cut of one $f_{out}(E, \Theta, \Phi = 0^{\circ})$, constructed from simulated observations of plasma protons with $N_{\rm in} = 10~{\rm cm}^{-3}$, $V_{\rm in} = 600~{\rm km~s}^{-1}$, and $k_{\rm B}T_{\rm in} = 60~{\rm eV}$. Figure 4(b) shows the input distribution $f(E,\Theta,\Phi=0^{\circ})$ for the same plasma parameters, and Fig. 4(c) shows the residual distribution $F_{\text{residual}}(E,\Theta,\Phi=0^{\circ})$. For this set of input plasma parameters, the distribution extends beyond the elevation field of view. At first glance, $f_{\text{out}}(E, \Theta, \Phi = 0^{\circ})$ and $f(E, \Theta, \Phi = 0^{\circ})$ appear very similar. However, $F_{\text{residual}}(E, \Theta, \Phi = 0^{\circ})$ is negative at the core (at velocities near the peak of f and f_{out}) and positive at the tails (velocities away from the peak). This is implying that the peak of $f_{\text{out}}(E,\Theta,\Phi=0^{\circ})$ is less than the peak of $f(E,\Theta,\Phi=0^{\circ})$. On the other hand, $f_{\text{out}}(E, \Theta, \Phi = 0^{\circ})$ is greater than $f(E, \Theta, \Phi = 0^{\circ})$ at the tails. Panels (d)–(f) show $f_{out}(E, \Theta, \Phi = 0^{\circ})$, $f(E, \Theta, \Phi = 0^{\circ})$, and their residuals $F_{\rm residual}(E,\Theta,\Phi=0^{\circ})$ for protons with the same density, but for $V_{\rm in}=800~{\rm km~s}^{-1}$ and $k_{\rm B}T_{\rm in}=30~{\rm eV}$. For this set of input parameters, the distribution function does not extend beyond the instrument's field of view. Similarly to the previous example, fout underestimates the core and overestimates the tails of the input distribution. In this case, we can directly observe differences between $f_{\rm out}$ and f, by comparing panels (d) and (e). Moreover, $F_{\rm residual}(E,\Theta,\Phi=0^\circ)$ in Fig. 4(f) extends to bigger absolute values than the corresponding $F_{\text{residual}}(E, \Theta, \Phi = 0^{\circ})$ of the slower and hotter plasma example shown in Fig. 4(c).

We complete our evaluations by calculating the mean residuals R [Eq. (11)] for a wide range of input solar wind proton bulk speeds $V_{\rm in}$ and temperatures $T_{\rm in}$, typical for protons in the inner heliosphere.³⁴ For all simulations, we use $N_{\rm in}=10~{\rm cm}^{-3}$. For each set of input plasma parameters, we simulate 10 samples. Thus, for each $V_{\rm in}-T_{\rm in}$ set, we calculate ten R values and, eventually, their average \overline{R} (average over the ten samples). Figure 5 shows \overline{R} as a function

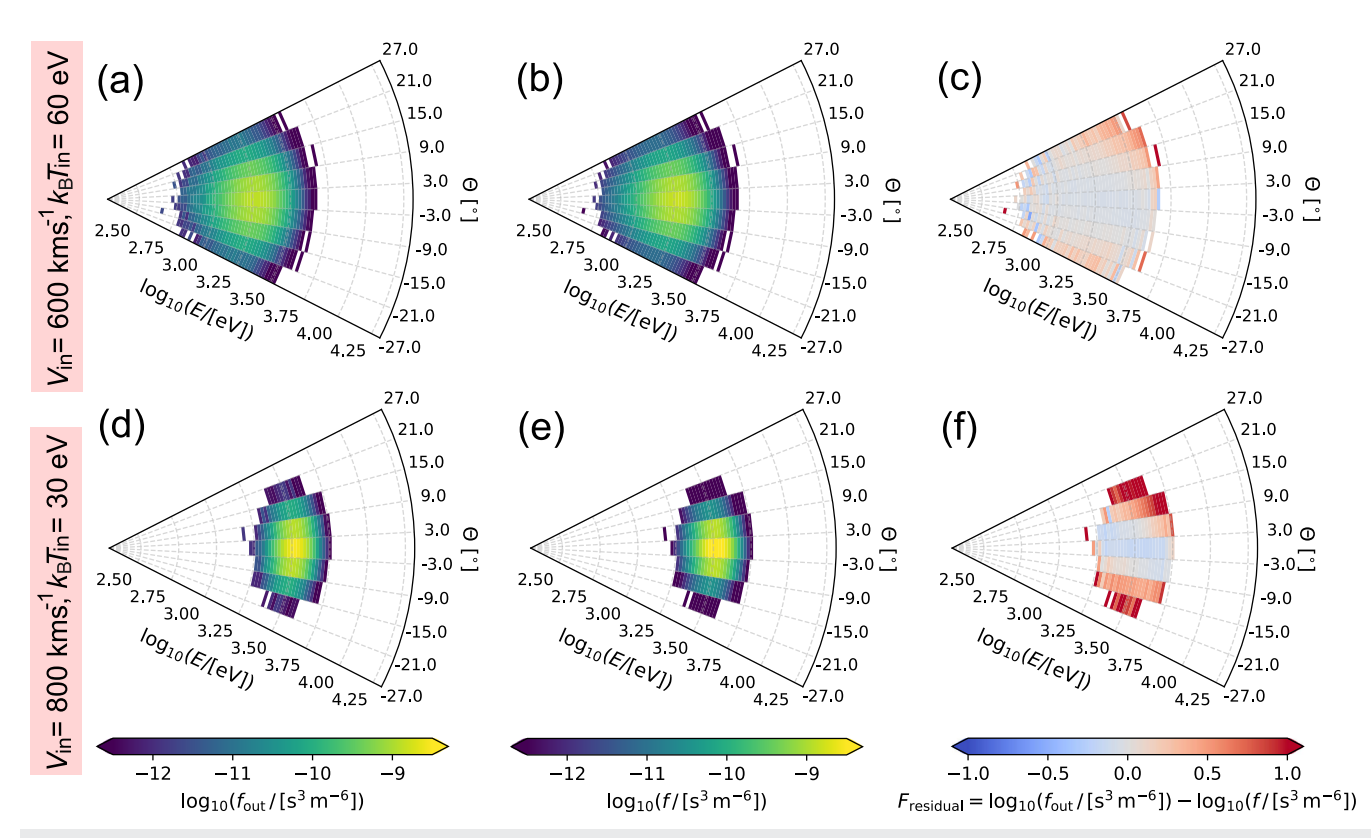


FIG. 4. 2D cuts of a (a) constructed $f_{\text{out}}(E,\Theta,\Phi=0^{\circ})$, (b) input $f(E,\Theta,\Phi=0^{\circ})$, and (c) the residual $F_{\text{residual}}(E,\Theta,\Phi=0^{\circ})$ distributions, for simulated plasma with $N_{\rm in} = 10~{\rm cm}^{-3}$, $V_{\rm in} = 600~{\rm km~s}^{-1}$, and $k_{\rm B}T_{\rm in} = 60~{\rm eV}$. Panels (d)–(f) are the corresponding distributions for plasma with the same density but $V_{\rm in} = 800~{\rm km~s}^{-1}$ and $k_B T_{in} = 30 \text{ eV}.$

of $V_{\rm in}$ and $T_{\rm in}$. The white curves are contours of selected \overline{R} values. We observe that \overline{R} increases with increasing speed and/or decreasing temperature. For the fastest ($V_{in} = 1000 \text{ km s}^{-1}$) and coldest $(k_B T_{in} = 5 \text{ eV})$ distributions we examine here, \overline{R} is greater than 3.5. This means that for this set of input parameters, the difference between the constructed and input distributions is several orders of

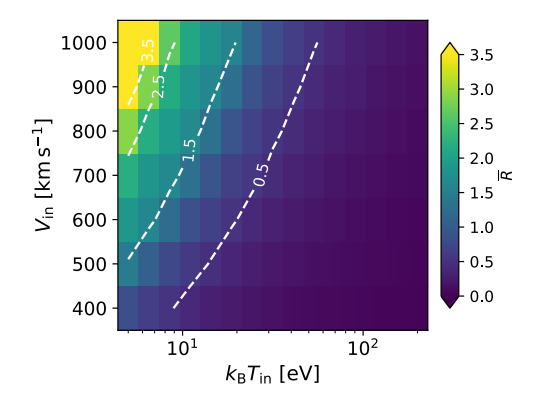


FIG. 5. 2D histogram of the averaged residuals \overline{R} as functions of the input speed $V_{\rm in}$ and temperature $k_{\rm B}T_{\rm in}$. The white dashed lines are contours of selected \overline{R} values (see the text for details).

magnitude, on average. Even for a relatively slow solar wind with $V_{\rm in} = 400 \ {\rm km \ s^{-1}}$, we see a rather significant difference ($\overline{R} > 0.5$) for temperatures $k_{\rm B}T_{\rm in}$ < 9 eV.

In Figs. 6(a)-6(c), we show 2D histograms of the average output density, speed, and temperature (average of the values determined for each of the 10 simulated samples per $V_{\rm in}$ – $T_{\rm in}$ set), divided by the corresponding moment of the input distribution, for each set of input parameters. In all panels, the ratios are ~1 for the smallest bulk speed and the largest plasma temperature we examine here, which are $V_{\rm in} = 400 \text{ km s}^{-1}$ and $T_{\rm in} = 200 \text{ eV}$, respectively. According to Fig. 6(a), as the proton speed increases and/or the plasma proton temperature decreases, the constructed distribution integrates to a smaller density than the one underlying the input distribution. There are examples within the examined range of parameters, for which the density determined by f_{out} is underestimated by more than 50% $(\log_{10}(\frac{N_{\text{out}}}{N_c}) < -0.3)$. According to Fig. 6(b), there is negligible difference between the speed determined by f_{out} and the speed underlying f. For all $V_{\rm in}$ – $T_{\rm in}$ that we examine here, the difference is much less than 1% ($\log_{10}\left(\frac{\overline{V}_{\text{out}}}{V_f}\right) < -0.001$). According to Fig. 6(c), the temperatures determined by f_{out} are significantly overestimated for a wide range of input speeds and temperatures. For instance, even for the slowest solar wind case ($V_{\rm in} \sim 400~{\rm km~s}^{-1}$), the temperature ratio is greater than 1.12 $(\log_{10}(\frac{T_{\text{out}}}{T_f}) > 0.05)$ for all input temperatures

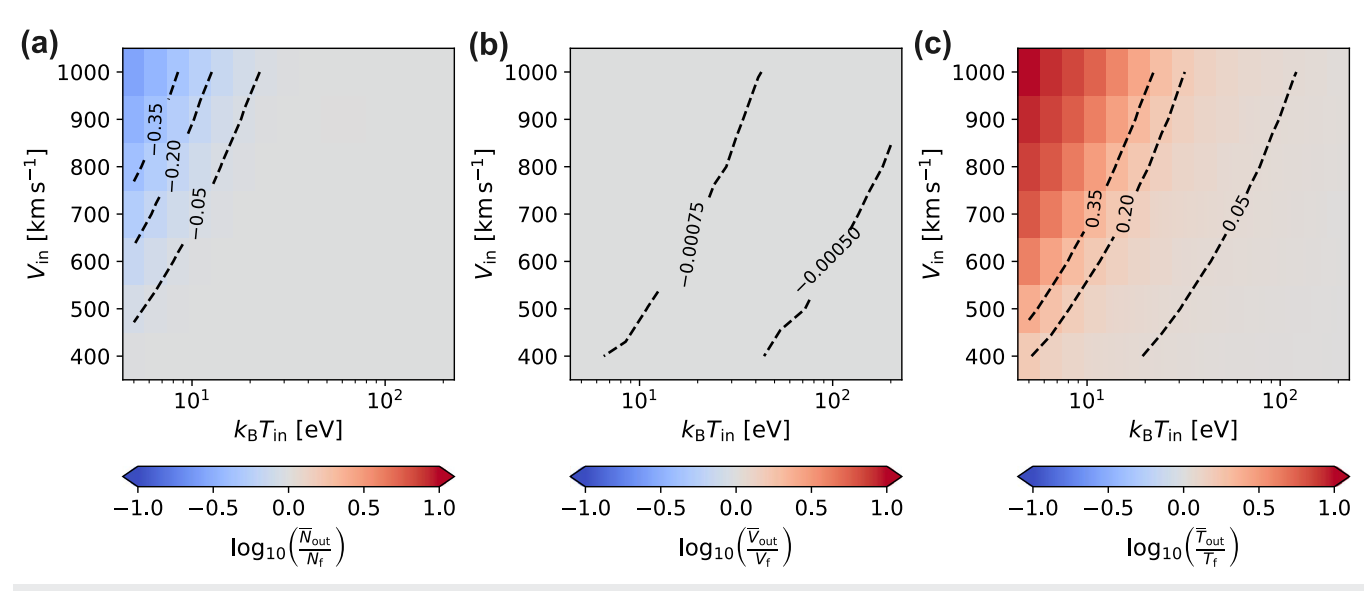


FIG. 6. Ratios of the plasma parameters determined from the constructed distributions, over the corresponding parameters underlying the input distributions; 2D histograms of (a) $\log_{10}\left(\frac{\overline{N}_{out}}{N_{c}}\right)$, (b) $\log_{10}\left(\frac{\overline{V}_{out}}{V_{c}}\right)$, and (c) $\log_{10}\left(\frac{\overline{T}_{out}}{T_{c}}\right)$ as functions of V_{in} and T_{in} . The black dashed curves are contours of selected ratio values.

less than 20 eV. For the fastest and coldest solar wind example we simulate here, the temperature is overestimated by a factor of ten.

V. DISCUSSION

Our results show that the interpretation of plasma observations by electrostatic analyzers may suffer significant inaccuracies, caused by the incapability of instruments to resolve the shape of the plasma VDFs within the instrument's energy, and/or angular bins. We model single-species plasma observations by an electrostatic analyzer concept and demonstrate that these systematic errors are larger as the bulk speed increases and/or the temperature decreases (see Fig. 5).

Under the same plasma conditions, observations by analyzers with lower resolution will return VDFs with larger uncertainties. When we refer to the instrument resolution in this study, we refer to the widths of the transmission curves along ε , θ , and ϕ , which are given by σ_E , σ_{Θ} , and σ_{Φ} , respectively (see Sec. III C). Therefore, for each instrument with specific energy and angular acceptance widths, there is a certain range of plasma parameters for which the constructed VDFs are reliable. We argue that in order to guarantee the validity of science studies, it is important to estimate the confidence level of the VDFs and their products that are determined from ESA observations. Such evaluation is possible by applying the same methodology that we present here to specific ESAs and plasma distribution functions.

A. VDF shape and instrument resolution

In Fig. 7, we demonstrate how the unresolved shape of the VDFs within the instrument's bins causes the systematic uncertainties we examine in this study. Panels (a) and (b) show two examples of an input distribution function shape along one of the sampled parameters (either energy or angle) within a single bin. Panel (c) shows the Gaussian response as a function of the sampled parameter within the bin. In the example shown in Fig. 7(a), the input distribution function increases as the sampled parameter increases. However, the positive gradient of the distribution decreases (negative second-order derivative). This results in an asymmetric distribution with respect to its value at the center of the bin. The bigger contribution to the flux integral [Eq. (3)] comes from f values that are smaller than the value of f at the center of the bin. As a consequence, the observed number of counts is smaller than the counts according to Eq. (8) using the value of f at the center of the bin. Therefore, f_{out} constructed with Eq. (9) underestimates the actual distribution f at the bin center.

The case shown in Fig. 7(b) has a positive second-order derivative. In this case, the asymmetry of the distribution results in a larger number of counts compared to those that Eq. (8) estimates with the value of f at the bin center. As a result, Eq. (9) overestimates the VDF.

In Appendix C, we derive the Taylor series of an isotropic Maxwellian VDF $f(\varepsilon, \theta, \phi)$, up to second-order terms, and evaluate it at the instrument bin centers E, Θ, Φ . We demonstrate that up to second-order terms, the systematic differences between f_{out} and fare approximately

$$\delta f(E,\Theta,\Phi) \approx \frac{1}{2} \left[\sigma_E^2 \frac{\partial^2 f}{\partial \varepsilon^2} (E,\Theta,\Phi) + \sigma_\Theta^2 \frac{\partial^2 f}{\partial \theta^2} (E,\Theta,\Phi) + \sigma_\Phi^2 \frac{\partial^2 f}{\partial \phi^2} (E,\Theta,\Phi) \right], \tag{12}$$

which implies that indeed the systematic uncertainties increase with increasing second-order derivatives of f. Equation (12) shows that for the same f, the uncertainties increase with increasing σ_E , σ_{Θ} , and

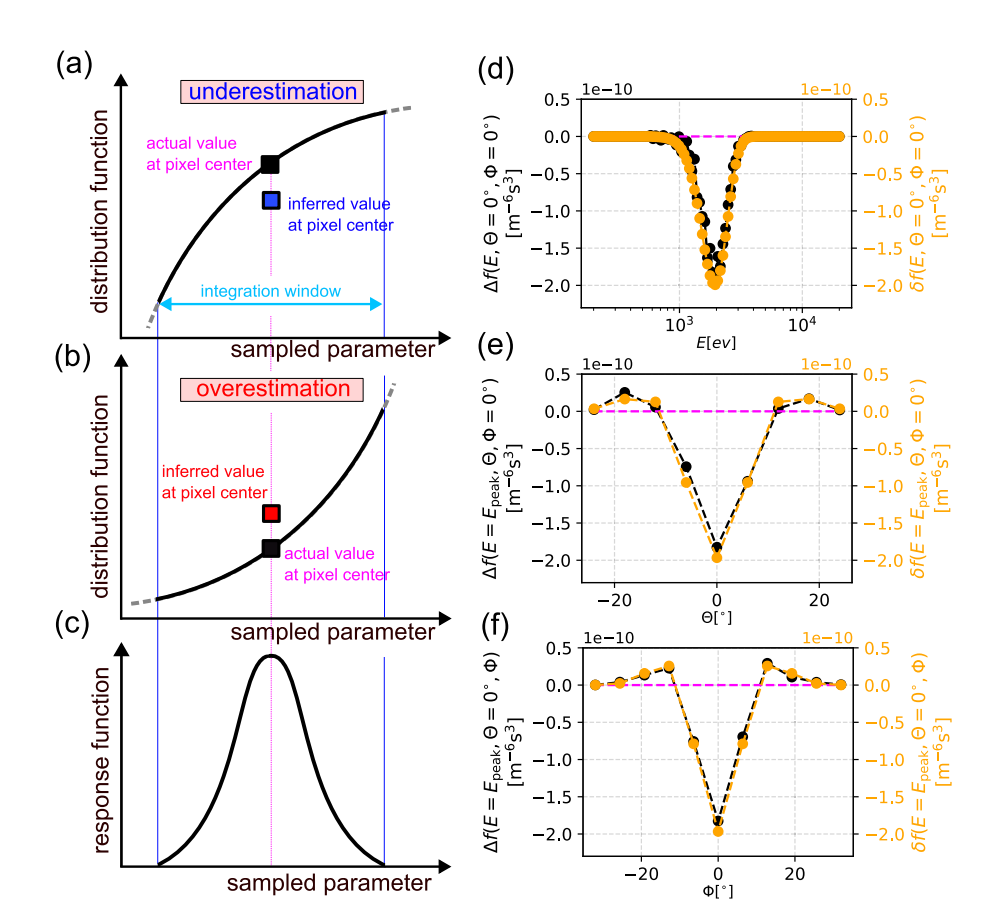


FIG. 7. (a) Example of a distribution function that has a negative second-order derivative with respect to the sampled parameter within the bin, which results in an underestimation of the distribution, and (b) an example of a distribution with positive second-order derivative with respect to the sampled parameter within the bin, which results in an overestimation of the plasma distribution. (c) A symmetric, Gaussian response function of a bin along the sampled parameter. (d) 1D cuts of the difference between the constructed and input plasma VDFs, Δf (black), and the analytical expression δf (orange), as functions of energy and for the elevation and azimuth of the peak, considering plasma with $N_{\rm in}=10~{\rm cm}^{-3}$, $V_{\rm in}=600~{\rm km~s}^{-1}$, and $k_{\rm B}T_{\rm in}=60~{\rm eV}$. (e) 1D cuts of Δf and δf , as functions of the elevation flow direction, at the energy and azimuth of the peak, and (f) 1D cuts of Δf and δf , as functions of the azimuth flow direction, at the energy and elevation direction of the peak, for the same plasma conditions.

 σ_{Φ} , which determine the instrument's energy and angular resolution. Appendix C shows the derivation of Eq. (12) and the analytical expressions for the derivatives of f.

In Figs. 7(d)–7(f), we compare 1D curves of the analytical δf function with the corresponding 1D cuts of

$$\Delta f(E, \Theta, \Phi) = f_{\text{out}}(E, \Theta, \Phi) - f(E, \Theta, \Phi). \tag{13}$$

The black curve in Fig. 7(d) is an 1D cut of Δf at the elevation and azimuth bins for which the distribution has its peak, i.e., $\Delta f(E,$ $\Theta = 0^{\circ}, \Phi = 0^{\circ}$), and considering plasma with $N_{\rm in} = 10 \text{ cm}^{-3}$, $V_{\rm in}$ = 600 km s⁻¹, and $k_B T_{in}$ = 60 eV. The orange curve in the same panel shows the 1D cut $\delta f(E, \Theta = 0^{\circ}, \Phi = 0^{\circ})$, calculated analytically under the same plasma conditions. In Fig. 7(e), we show $\Delta f(E = E_{\text{peak}}, \Theta, \Phi = 0^{\circ})$ and $\delta f(E = E_{\text{peak}}, \Theta, \Phi = 0^{\circ})$ under the same plasma conditions, which are the 1D cuts of Δf and δf , at the energy and azimuth bins that capture the peak of f, respectively. Figure 7(f) shows the corresponding 1D cuts at $E = E_{peak}$ and $\Theta = 0^{\circ}$. The apparent similarity between Δf and δf confirms that Eq. (12) successfully estimates the uncertainties in this example. As the higher-order derivatives of the VDF increase (colder and/or faster species), and as the instrument resolution decreases (larger σ_E , σ_{Θ} , σ_{Φ}), Eq. (12) would require higher-order terms to describe the uncertainties. In Appendix C, we explain the approach behind the derivation of Eq. (12), which is useful for fast and easy diagnosis of the level of expected uncertainties.

B. Impact on plasma physical parameters

Figure 4 shows that the constructed distributions, in general, underestimate the core of the input distribution functions, while they overestimate their tails. This is in agreement with the diagrams shown in Figs. 7(d)-7(f). It is also consistent with the fact that in colder and faster plasmas, the plasma density is underestimated and the temperature is overestimated (Fig. 6). The core of the distribution contributes significantly to the zeroth-order velocity moment (the particle density), while the tails contain the higher energy particles, which make a significant contribution to the second-order velocity moment (the temperature of the species). The bulk speed accuracy is barely affected in the examples we examine here. Even in the colder and faster plasma examples we examine, and for the specific instrument resolution, the residuals are approximately symmetric around the bulk (see Figs. 4 and 7) and thus the first-order velocity moment is barely affected. We do not expect this to hold for any type of f or for bigger σ_E . This study does not examine the accuracy of the recovered plasma parameters for different plasma bulk velocity directions. Given the typical Gaussian response of the individual elevation and azimuth bins, we expect different distribution of counts as a cold/fast proton beam shifts in direction (in sub-bin scales). This is the subject of an ongoing, independent research by L. Berger et al., which focuses on the temperature uncertainties as functions of the plasma direction, considering the proton plasma observations by Solar Orbiter (personal communication).

We acknowledge that the systematic errors in the VDF shapes can have a vital impact on scientific studies that require detailed knowledge of plasma VDFs.²⁵ Our results demonstrate that the VDF shape of cold and fast solar wind protons is highly affected, even by orders of magnitude. This systematic uncertainty is a function of the input plasma, and thus, it is expected to lead to erroneous correlations between the plasma parameters; i.e., artificially larger VDF tails in colder and faster wind. There are cases within the range of plasma parameters we examine, in which the systematic uncertainties of this type exceed significantly the statistical and systematic uncertainties of different sources, such as background noise, ^{15,17} plasma fluctuations, ²¹ count uncertainties, ^{12,35} limited sampling, ³¹ and the incapability to distinct between VDFs of different species. ²³

We highlight that a critical evaluation of the uncertainties in specific applications should account for the VDFs of all the species that the instrument detects. For instance, ESAs in the solar wind and planetary magnetosheaths capture the distributions of alpha particles along with those of the protons. $^{36-39}$ For co-moving proton and alpha populations, the VDFs of alphas extend at higher energy-per-charge bins than those recording the proton VDFs due to their higher bulk energy-per-charge at the same velocities. Higher energy-per-charge bins, however, have larger σ_E and thus, even if the VDFs of the two species had the same shape and even if the analysis could distinguish between the two species, the VDFs of alphas would be resolved with larger systematic uncertainty compared to protons.

C. Potential mitigations

One popular technique to determine the plasma VDFs is by fitting the observations to forward model predictions. ^{9,31,40} With this technique, we can optimize the parameters of analytical VDF models to reproduce the actual observations. We argue that the use of high-resolution forward models, which take into account the detailed response function of the instruments and the VDF shapes on sub-bin scales as we describe in Sec. III C, can overcome the systematic uncertainties arising from the instrument's finite resolution. Although this is one possible way to recover the actual VDFs, it requires a detailed implementation of the instrument's response function per bin and a numerical calculation on sub-bin scales.

Solar wind protons usually exhibit non-thermal features, such as beams and supra-thermal tails, $^{41-43}$ and an accurate forward modeling would require numerous iterations with a variety of input f functions, beyond the isotropic Maxwell distribution. The users of forward models should keep in mind that the optimization of VDF models that do not correspond to the actual plasma VDF leads to systematic errors. 27 In addition, classic fitting techniques that are used for optimizing models to observations may introduce biases and lead to systematic errors and artificial correlations between the determined plasma parameters. 11,13,14

The results of this study are linked to the specific instrument model and under the specific plasma conditions we consider for our demonstrations, which are described in Sec. III. Our purpose is to notify the community that the accurate determination of plasma parameters from *in situ* observations requires a thorough examination of the possible VDFs and knowledge of the instrument response function and resolution. The same technique we describe here can

be adapted to evaluate the performance of any analyzer of a similar design, under any plasma conditions.

ACKNOWLEDGMENTS

C.I. acknowledges support from STFC Ph.D. Studentship under Grant No. ST/X508858/1. C.J.O. and D.V. acknowledge support from STFC Consolidated under Grant No. ST/W001004/1. This work was partially supported by the Royal Society (UK) and the Consiglio Nazionale delle Ricerche (Italy) through the International Exchanges Cost Share scheme/Joint Bilateral Agreement project "Multi-scale electrostatic energization of plasmas: comparison of collective processes in laboratory and space" (Award Nos. IEC\R2\222050 and SAC.AD002.043.021). G.N. acknowledges helpful discussions on this topic with Lynn B Wilson III.

AUTHOR DECLARATIONS

Conflict of Interest

The authors have no conflicts to disclose.

Author Contributions

G. Nicolaou: Conceptualization (lead); Formal analysis (lead); Investigation (lead); Methodology (lead); Validation (lead); Visualization (lead); Writing – original draft (lead); Writing – review & editing (equal). C. Ioannou: Investigation (supporting); Methodology (supporting); Visualization (supporting); Writing – review & editing (equal). C. J. Owen: Data curation (equal); Investigation (supporting); Writing – review & editing (equal). D. Verscharen: Investigation (supporting); Writing – review & editing (supporting); Visualization (supporting); Writing – review & editing (supporting). A. Fedorov: Investigation (supporting); Methodology (supporting). P. Louarn: Investigation (supporting); Methodology (supporting).

DATA AVAILABILITY

The data that support the findings of this study are available from the corresponding author upon reasonable request.

APPENDIX A: MODEL OPTIMIZATION

The accuracy of the forward model increases as we increase the number of discrete ε_i , θ_j , and ϕ_k steps within the bin width, at which we evaluate the sum in Eq. (5). By increasing the number of steps, the computational time increases. Thus, we optimize the model by using the minimum number of steps required for accurate simulations. As shown in Fig. 1, colder and faster distributions require a model with higher resolution to maintain a high accuracy of the simulated counts. For our evaluation, we first use 33 steps for each parameter $(\varepsilon, \theta, \phi)$ to simulate the number of counts for an input Maxwellian with $N_{\rm in}=10~{\rm cm}^{-3}$, $V_{\rm in}=1000~{\rm km~s}^{-1}$ along $\hat{\Theta}=\Phi=0^{\circ}$, and $T_{\rm in} = 1$ eV. We also set $\alpha_0 = 1$ m² in order to have counts recorded by many instrument bins. We use this simulation product as the high-resolution reference model (M33 model product). We then simulate measurements with models of different resolutions, starting from a low number of ε_i , θ_i , and ϕ_k steps (same number of steps for each parameter) and simulate the number of counts of the same

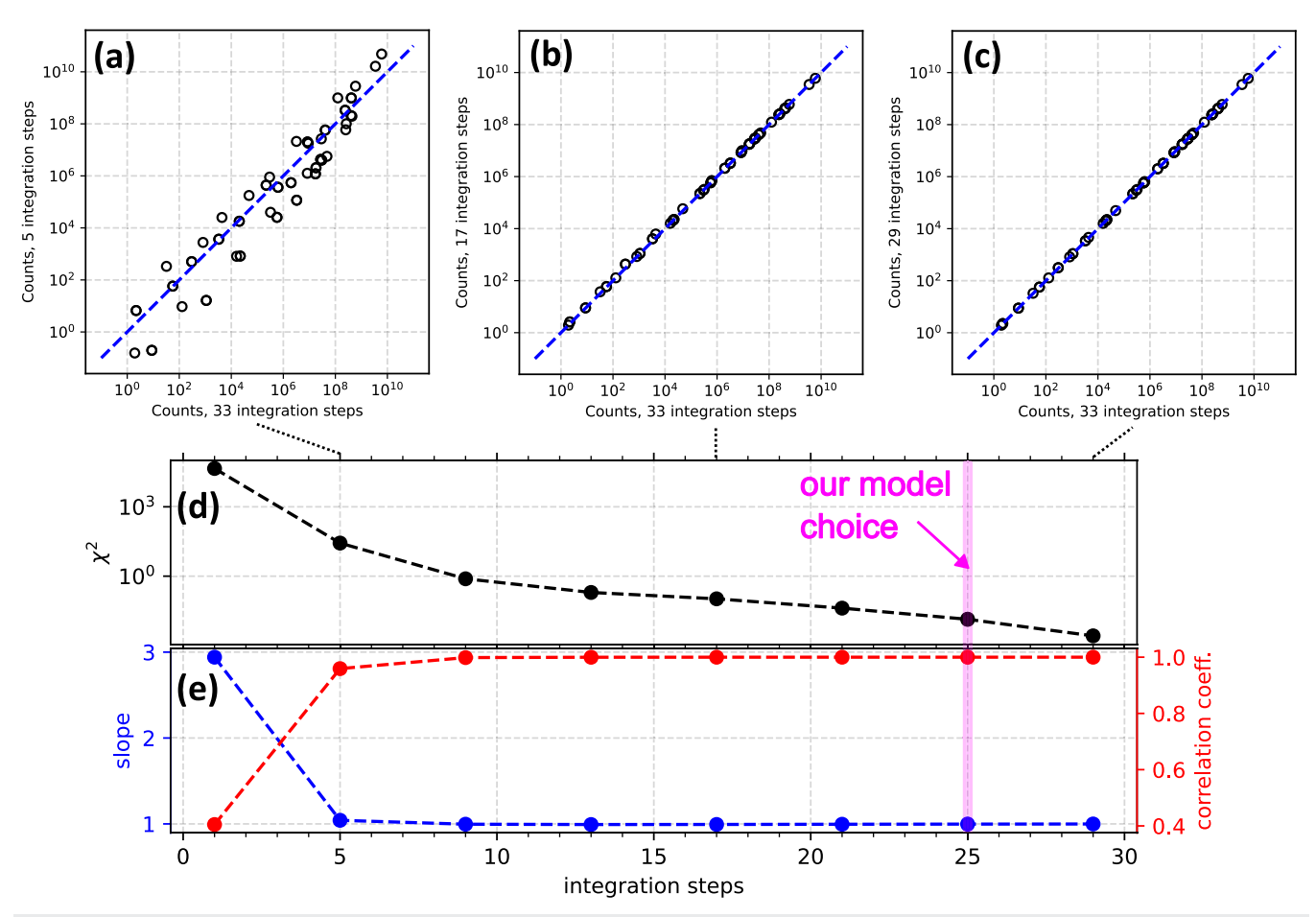


FIG. 8. Comparison of observations produced by models of different resolutions against the simulations of the M33 model. Number of counts simulated using (a) 5 integration steps, (b) 17, and (c) 29 integration steps, vs the number of counts simulated by M33 for the same input proton plasma parameters. (d) χ^2 value of simulated counts by models of different integration steps and the counts simulated by M33 and (e) the slope (blue) and the correlation coefficient (red) of the simulated counts by different models and M33, as functions of the integration steps of each model.

distribution function. We compare the output of each model to the product of M33. We calculate the chi-squared value χ^2 , the Pearson correlation coefficient, and the slope between the number of counts by each model and the M33 reference model.

In Fig. 8, we show the results of our model optimization. To optimize between computational time and accuracy, we use a model with 25 integration steps throughout this study, which produces virtually the same results as M33, for this fast and significantly cold Maxwellian we use for input. The model we use leads to $\chi^2 \sim 10^{-2}$ and it correlates almost perfectly with M33, since the Pearson correlation coefficient and the slope are both very close to 1.

APPENDIX B: VELOCITY MOMENTS

We calculate the output plasma bulk parameters as the velocity moments of the distribution function constructed from the

observations.^{23,31} The output plasma density is estimated by the 0th-order moment,

$$N_{\text{out}} = \sum_{i=1}^{96} \sum_{i=1}^{9} \sum_{k=1}^{11} \sqrt{2} f_{\text{out}}(E_i, \Theta_j, \Phi_k) \left(\frac{E_i}{m}\right)^{\frac{3}{2}} \cos \Theta_j \frac{\Delta E}{E} \Delta \Theta \Delta \Phi, \text{ (B1)}$$

where ΔE , $\Delta \Theta$, and $\Delta \Phi$ are the differences between consecutive energy, elevation, and azimuth bin centers, respectively. The energy bins are exponentially spaced, resulting in a constant $\frac{\Delta E}{E} \approx 0.05$, while the elevation and azimuth bins are uniformly spaced, such that $\Delta \Theta = 6^{\circ}$ and $\Delta \Phi = 6.4^{\circ}$. The first-order moments determine the bulk velocity components of the plasma,

$$V_{x,\text{out}} = \frac{1}{N_{\text{out}}} \sum_{i=1}^{96} \sum_{j=1}^{9} \sum_{k=1}^{11} 2f_{\text{out}}(E_i, \Theta_j, \Phi_k) \left(\frac{E_i}{m}\right)^2$$

$$\times \cos^2 \Theta_j \cos \Phi_k \frac{\Delta E}{F} \Delta \Theta \Delta \Phi, \tag{B2}$$

$$V_{y,\text{out}} = \frac{1}{N_{\text{out}}} \sum_{i=1}^{96} \sum_{j=1}^{9} \sum_{k=1}^{11} 2f_{\text{out}}(E_i, \Theta_j, \Phi_k) \left(\frac{E_i}{m}\right)^2$$

$$\times \cos^2 \Theta_j \sin \Phi_k \frac{\Delta E}{E} \Delta \Theta \Delta \Phi, \tag{B3}$$

and

$$\begin{split} V_{\rm z,out} &= \frac{1}{N_{\rm out}} \sum_{i=1}^{96} \sum_{j=1}^{9} \sum_{k=1}^{11} 2f_{\rm out}(E_i, \Theta_j, \Phi_k) \left(\frac{E_i}{m}\right)^2 \\ &\times \cos\Theta_j \sin\Theta_j \frac{\Delta E}{F} \Delta\Theta \Delta \Phi, \end{split} \tag{B4}$$

from which we obtain the bulk speed,

$$V_{\text{out}} = \sqrt{V_{\text{x,out}}^2 + V_{\text{y,out}}^2 + V_{\text{z,out}}^2}.$$
 (B5)

The second-order moment determines the scalar temperature,

$$k_{\rm B}T_{\rm out} = \frac{1}{3N_{\rm out}} \sum_{i=1}^{96} \sum_{j=1}^{9} \sum_{k=1}^{11} \sqrt{\frac{2}{m}} \left(w_{{\rm x},ijk}^2 + w_{{\rm y},ijk}^2 + w_{{\rm z},ijk}^2 \right) \times f_{\rm out}(E_i, \Theta_j, \Phi_k) E_i^{\frac{3}{2}} \cos \Theta_j \frac{\Delta E}{E} \Delta \Theta \Delta \Phi,$$
 (B6)

where

$$w_{x,ijk} = \sqrt{\frac{2E_i}{m}}\cos\Theta_j\cos\Phi_k - V_{x,\text{out}},\tag{B7}$$

$$w_{y,ijk} = \sqrt{\frac{2E_i}{m}}\cos\Theta_j\sin\Phi_k - V_{y,\text{out}},$$
 (B8)

and

$$w_{z,ijk} = \sqrt{\frac{2E_i}{m}} \sin \Theta_j - V_{z,\text{out}}.$$
 (B9)

By replacing $f_{\text{out}}(E, \Theta, \Phi)$ with $f(E, \Theta, \Phi)$ in the equations above, we calculate N_f , V_f , and T_f , which are the density, speed, and temperature moments of the input distribution, respectively.

APPENDIX C: TAYLOR SERIES OF THE INTEGRATED DISTRIBUTION FUNCTION

The Taylor expansion of $f(\varepsilon, \theta, \phi)$ at the center of each instrument bin $\varepsilon = E, \theta = \Theta, \phi = \Phi$, up to second-order terms, is

$$f(\varepsilon,\theta,\phi) \approx f(E,\Theta,\Phi) + \frac{\partial f}{\partial \varepsilon}(E,\Theta,\Phi)(\varepsilon-E) + \frac{\partial f}{\partial \theta}(E,\Theta,\Phi)(\theta-\Theta) + \frac{\partial f}{\partial \phi}(E,\Theta,\Phi)(\phi-\Phi) + \frac{1}{2} \left[\frac{\partial^2 f}{\partial \varepsilon^2}(E,\Theta,\Phi)(\varepsilon-E)^2 + \frac{\partial^2 f}{\partial \theta^2}(E,\Theta,\Phi)(\theta-\Theta)^2 + \frac{\partial^2 f}{\partial \phi^2}(E,\Theta,\Phi)(\phi-\Phi)^2 \right] + \frac{\partial^2 f}{\partial \varepsilon \partial \theta}(E,\Theta,\Phi)(\varepsilon-E)(\theta-\Theta) + \frac{\partial^2 f}{\partial \varepsilon \partial \phi}(E,\Theta,\Phi)(\varepsilon-E)(\theta-\Theta) + \frac{\partial^2 f}{\partial \theta \partial \phi}(E,\Theta,\Phi)(\theta-\Theta)(\phi-\Phi).$$
 (C1)

By using the Taylor expansion of $f(\varepsilon,\theta,\Phi)$, the integral in Eq. (3) becomes

$$C_{\exp}(E,\Theta,\Phi) \approx \Delta \tau \int_{\varepsilon_{\min}}^{\varepsilon_{\max}} \int_{\theta_{\min}}^{\theta_{\max}} \int_{\phi_{\min}}^{\phi_{\max}} \alpha(E,\Theta,\Phi,\varepsilon,\theta,\phi) \bigg[f(E,\Theta,\Phi) \\ + \cdots + \frac{\partial^{2} f}{\partial \theta \partial \phi} (E,\Theta,\Phi) (\theta - \Theta) (\phi - \Phi) \bigg] \\ \times \frac{2}{m^{2}} \varepsilon \, d\varepsilon \, \cos \, \theta \, d\theta \, d\phi.$$
 (C2)

We now replace the linear ε term with its value at the center of the bin E and we write

$$C_{\exp}(E,\Theta,\Phi) \approx \frac{2E^2 \Delta \tau}{m^2} \int_{\epsilon_{\min}}^{\epsilon_{\max}} \int_{\theta_{\min}}^{\theta_{\max}} \int_{\phi_{\min}}^{\phi_{\max}} \alpha(E,\Theta,\Phi,\epsilon,\theta,\phi)$$

$$\times \left[f(E,\Theta,\Phi) + \dots + \frac{\partial^2 f}{\partial \theta \partial \phi}(E,\Theta,\Phi)(\theta-\Theta)(\phi-\Phi) \right]$$

$$\times \frac{d\epsilon}{E} \cos \theta \, d\theta \, d\phi, \qquad (C3)$$

which can be realized as the sum of integrals for each term of the Taylor series. The first integral, which is the integral containing the first term $f(E, \Theta, \Phi)$, is

$$\frac{2E^{2}\Delta\tau}{m^{2}}f(E,\Theta,\Phi)\int_{\epsilon_{\min}}^{\epsilon_{\max}}\int_{\theta_{\min}}^{\theta_{\max}}\int_{\phi_{\min}}^{\phi_{\max}}\alpha(E,\Theta,\Phi,\epsilon,\theta,\phi)\frac{d\epsilon}{E}\cos\theta\,d\theta\,d\phi$$

$$=\frac{2E^{2}\Delta\tau G(E,\Theta,\Phi)f(E,\Theta,\Phi)}{m^{2}},$$
(C4)

which is identical to Eq. (8). As a result, the integrals of the higherorder terms of $f(\varepsilon, \theta, \phi)$ estimate the discrepancy between the simplified, zeroth-order approach in Eq. (8), and the exact number of counts given by Eq. (3), which quantifies the systematic uncertainties we investigate here. For a symmetric response function $\alpha(E, \Theta, \Phi, \varepsilon, \theta, \phi)$ cos θ around the bin center E, Θ, Φ , we get

$$\langle \varepsilon \rangle = \frac{\int\limits_{\varepsilon_{\min}}^{\varepsilon_{\max}} \int\limits_{\theta_{\min}}^{\theta_{\max}} \int\limits_{\phi_{\min}}^{\phi_{\max}} \varepsilon \alpha(E, \Theta, \Phi, \varepsilon, \theta, \phi) \frac{d\varepsilon}{E} \cos \theta \, d\theta \, d\phi}{\int\limits_{\varepsilon_{\min}}^{\varepsilon_{\max}} \int\limits_{\theta_{\min}}^{\theta_{\max}} \int\limits_{\phi_{\min}}^{\phi_{\max}} \int\limits_{\phi_{\min}}^{\phi_{\max}} \alpha(E, \Theta, \Phi, \varepsilon, \theta, \phi) \frac{d\varepsilon}{E} \cos \theta \, d\theta \, d\phi} = E, \quad (C5)$$

$$\langle \theta \rangle = \frac{\int\limits_{\varepsilon_{\min}}^{\varepsilon_{\max}} \int\limits_{\theta_{\min}}^{\theta_{\max}} \int\limits_{\phi_{\min}}^{\phi_{\max}} \theta \alpha(E, \Theta, \Phi, \varepsilon, \theta, \phi) \frac{d\varepsilon}{E} \cos \theta \, d\theta \, d\phi}{\int\limits_{\varepsilon_{\min}}^{\varepsilon_{\max}} \int\limits_{\theta_{\min}}^{\theta_{\max}} \int\limits_{\phi_{\min}}^{\phi_{\max}} \alpha(E, \Theta, \Phi, \varepsilon, \theta, \phi) \frac{d\varepsilon}{E} \cos \theta \, d\theta \, d\phi} = \Theta,$$
(C6)

and

$$\langle \phi \rangle = \frac{\int_{\epsilon_{\min}}^{\epsilon_{\max}} \int_{\theta_{\min}}^{\theta_{\max}} \phi_{\alpha}(E, \Theta, \Phi, \varepsilon, \theta, \phi) \frac{d\varepsilon}{E} \cos \theta \, d\theta \, d\phi}{\int_{\epsilon_{\min}}^{\epsilon_{\min}} \int_{\theta_{\min}}^{\theta_{\max}} \phi_{\max}} \int_{\phi_{\min}}^{\phi_{\min}} \alpha(E, \Theta, \Phi, \varepsilon, \theta, \phi) \frac{d\varepsilon}{E} \cos \theta \, d\theta \, d\phi} = \Phi,$$
(C7)

and therefore, all first-order derivative terms that have $(\varepsilon - E)$, $(\theta - \Theta)$, and $(\phi - \Phi)$ go to zero and do not contribute to the uncertainty we investigate. For this reason, the second-order derivative terms with the mixed energy, elevation, and azimuth terms, also go to zero. As a result, the systematic uncertainty of the estimated counts δC_{exp} is approximately

$$\delta C_{\text{exp}}(E,\Theta,\Phi) \sim \frac{E^2 \Delta \tau}{m^2} \left[\frac{\partial^2 f}{\partial \varepsilon^2} (E,\Theta,\Phi) \int_{\varepsilon_{\text{min}}}^{\varepsilon_{\text{max}}} \int_{\theta_{\text{min}}}^{\theta_{\text{max}}} \int_{\phi_{\text{min}}}^{\varepsilon_{\text{max}}} (\varepsilon - E)^2 \alpha(E,\Theta,\Phi,\varepsilon,\theta,\phi) \frac{d\varepsilon}{E} \cos\theta \, d\theta \, d\phi \right. \\
+ \frac{\partial^2 f}{\partial \theta^2} (E,\Theta,\Phi) \int_{\varepsilon_{\text{min}}}^{\varepsilon_{\text{max}}} \int_{\phi_{\text{min}}}^{\theta_{\text{max}}} \int_{\phi_{\text{min}}}^{\phi_{\text{max}}} (\theta - \Theta)^2 \alpha(E,\Theta,\Phi,\varepsilon,\theta,\phi) \frac{d\varepsilon}{E} \cos\theta \, d\theta \, d\phi \\
+ \frac{\partial^2 f}{\partial \phi^2} (E,\Theta,\Phi) \int_{\varepsilon_{\text{min}}}^{\varepsilon_{\text{max}}} \int_{\theta_{\text{min}}}^{\theta_{\text{max}}} \int_{\phi_{\text{min}}}^{\phi_{\text{max}}} (\phi - \Phi)^2 \alpha(E,\Theta,\Phi,\varepsilon,\theta,\phi) \frac{d\varepsilon}{E} \cos\theta \, d\theta \, d\phi \right]. \tag{C8}$$

We can solve the above-mentioned integral, either numerically or analytically, for any input distribution and a known response function at each bin. At this point, we adopt one simplification and treat $\alpha \cos \theta$ [Eq. (4)] as it was a pure 3D-Gaussian, i.e.,

$$\alpha(E,\Theta,\Phi,\varepsilon,\theta,\phi)\cos\theta \approx \alpha_0 \exp\left[-\frac{\left(\frac{\varepsilon}{E}-1\right)^2}{2\left(\frac{\sigma_E}{E}\right)^2}\right] \exp\left[-\frac{(\theta-\Theta)^2}{2(\sigma_\Theta)^2}\right] \exp\left[-\frac{(\phi-\Phi)^2}{2(\sigma_\Phi)^2}\right]$$

$$= \alpha_0 \exp\left[-\frac{(\varepsilon-E)^2}{2(\sigma_E)^2}\right] \exp\left[-\frac{(\theta-\Theta)^2}{2(\sigma_\Theta)^2}\right] \exp\left[-\frac{(\phi-\Phi)^2}{2(\sigma_\Theta)^2}\right], \tag{C9}$$

for which the analytical solution of Eq. (C8) is straightforward. Under this approximation, we get

$$\begin{split} & \underset{\varepsilon_{\min}}{\varepsilon_{\max}} \int_{\theta_{\min}}^{\theta_{\max}} \int_{\phi_{\min}}^{\phi_{\max}} (\varepsilon - E)^2 \alpha(E, \Theta, \Phi, \varepsilon, \theta, \phi) \frac{\mathrm{d}\varepsilon}{E} \cos \theta \, \mathrm{d}\theta \, \mathrm{d}\phi \\ & \approx E^{-1} \alpha_0 (2\pi)^{3/2} \sigma_E^3 \sigma_\Theta \sigma_\Phi, \end{split} \tag{C10}$$

$$\int_{\varepsilon_{\min}}^{\varepsilon_{\max}} \int_{\theta_{\min}}^{\theta_{\max}} \int_{\phi_{\min}}^{\phi_{\max}} (\theta - \Theta)^{2} \alpha(E, \Theta, \Phi, \varepsilon, \theta, \phi) \frac{d\varepsilon}{E} \cos \theta \, d\theta \, d\phi$$

$$\approx E^{-1} \alpha_{0} (2\pi)^{3/2} \sigma_{E} \sigma_{\Theta}^{3} \sigma_{\Phi}, \tag{C11}$$

and

$$\int_{\varepsilon_{\min}}^{\varepsilon_{\max}} \int_{\theta_{\min}}^{\theta_{\max}} \int_{\phi_{\min}}^{\phi_{\max}} (\phi - \Phi)^{2} \alpha(E, \Theta, \Phi, \varepsilon, \theta, \phi) \frac{d\varepsilon}{E} \cos \theta \ d\theta \ d\phi$$

$$\approx E^{-1} \alpha_{0} (2\pi)^{3/2} \sigma_{E} \sigma_{\Theta} \sigma_{\Phi}^{3}, \tag{C12}$$

and by substituting back to Eq. (C8), we get

$$\delta C_{\text{exp}}(E,\Theta,\Phi) = \frac{\alpha_0 (2\pi)^{\frac{3}{2}} \sigma_E \sigma_\Theta \sigma_\Phi E \Delta \tau}{m^2} \left[\sigma_E^2 \frac{\partial^2 f}{\partial \varepsilon^2} (E,\Theta,\Phi) + \sigma_\Theta^2 \frac{\partial^2 f}{\partial \theta^2} (E,\Theta,\Phi) + \sigma_\Phi^2 \frac{\partial^2 f}{\partial \phi^2} (E,\Theta,\Phi) \right]. \quad (C13)$$

Under the 3D-Gaussian response approximation [Eq. (C9)], the geometric factor of the instrument is approximately,

$$G(E,\Theta,\Phi) \approx \alpha_0 (2\pi)^{\frac{3}{2}} \frac{\sigma_E}{F} \sigma_\Theta \sigma_\Phi,$$
 (C14)

and thus, Eq. (C13) becomes

$$\delta C_{\text{exp}}(E,\Theta,\Phi) = \frac{G(E,\Theta,\Phi)E^2\Delta\tau}{m^2} \left[\sigma_E^2 \frac{\partial^2 f}{\partial \varepsilon^2} (E,\Theta,\Phi) + \sigma_\Theta^2 \frac{\partial^2 f}{\partial \theta^2} (E,\Theta,\Phi) + \sigma_\Phi^2 \frac{\partial^2 f}{\partial \phi^2} (E,\Theta,\Phi) \right]. \quad (C15)$$

The conversion from observed counts to VDF using Eq. (9) results in a systematic offset in the estimation of f_{out} , given by

$$\delta f(E,\Theta,\Phi) = \frac{1}{2} \left[\sigma_E^2 \frac{\partial^2 f}{\partial \varepsilon^2} (E,\Theta,\Phi) + \sigma_\Theta^2 \frac{\partial^2 f}{\partial \theta^2} (E,\Theta,\Phi) + \sigma_\Phi^2 \frac{\partial^2 f}{\partial \phi^2} (E,\Theta,\Phi) \right], \tag{C16}$$

where σ_E , σ_Θ , and σ_Φ determine the energy, elevation, and azimuth acceptance widths of the instrument bin, respectively. In general, σ_E , σ_Θ , and σ_Φ are parameters that must be determined for each individual bin. For our concept instrument, we assume the same set of σ_E/E , σ_Θ , and σ_Φ for all the bins, which does not affect the validity of the analysis we perform here. With a close look at Eq. (C16), we understand that the systematic uncertainty increases with increasing second-order derivatives of f and also with increasing acceptance widths (decreasing resolution) of the instrument.

We now evaluate δf analytically for certain plasma properties and our concept instrument. For plasma with bulk velocity along $\theta = \phi = 0^{\circ}$ direction, the Maxwell distribution in Eq. (2) becomes

$$f(\varepsilon, \theta, \phi) = Ae^{-\frac{\varepsilon + \varepsilon_0 - 2\sqrt{\varepsilon\varepsilon_0}\cos\theta\cos\phi}{k_B T_{\rm in}}},$$
 (C17)

where $A = N_{\rm in} \left(\frac{m}{2\pi k_{\rm B} T_{\rm in}}\right)^{\frac{3}{2}}$. Then, the partial derivative of f with respect to energy is

$$\frac{\partial f}{\partial \varepsilon} = \frac{1}{k_{\rm B} T_{\rm in}} \left(\sqrt{\frac{\varepsilon_0}{\varepsilon}} \cos \theta \cos \phi - 1 \right) A e^{-\frac{\varepsilon + \alpha_0 - 2\sqrt{\alpha_0} \cos \theta \cos \phi}{k_{\rm B} T_{\rm in}}} \\
= \frac{1}{k_{\rm B} T_{\rm in}} \left(\sqrt{\frac{\varepsilon_0}{\varepsilon}} \cos \theta \cos \phi - 1 \right) f;$$
(C18)

the partial derivative of f with respect to elevation is

$$\frac{\partial f}{\partial \theta} = \frac{-2\sqrt{\varepsilon\varepsilon_0}\sin\theta\cos\phi}{k_{\rm B}T_{\rm in}} Ae^{-\frac{\epsilon+\epsilon_0-2\sqrt{\varepsilon\varepsilon_0}\cos\theta\cos\phi}{k_{\rm B}T_{\rm in}}}$$

$$= \frac{-2\sqrt{\varepsilon\varepsilon_0}\sin\theta\cos\phi}{k_{\rm B}T_{\rm in}} f; \tag{C19}$$

and the partial derivative with respect to azimuth is

$$\frac{\partial f}{\partial \phi} = \frac{-2\sqrt{\varepsilon\varepsilon_0}\cos\theta\sin\phi}{k_{\rm B}T_{\rm in}} A e^{-\frac{\varepsilon+\varepsilon_0-2\sqrt{\varepsilon\varepsilon_0}\cos\theta\cos\phi}{k_{\rm B}T_{\rm in}}}$$

$$= \frac{-2\sqrt{\varepsilon\varepsilon_0}\cos\theta\sin\phi}{k_{\rm B}T_{\rm in}} f. \tag{C20}$$

The second-order partial derivative of f with respect to energy is

$$\frac{\partial^2 f}{\partial \varepsilon^2} = -\frac{\sqrt{\varepsilon_0} \cos \theta \cos \phi}{2k_{\rm B} T_{\rm in} \varepsilon^{3/2}} f + \frac{1}{k_{\rm B} T_{\rm in}} \left(\sqrt{\frac{\varepsilon_0}{\varepsilon}} \cos \theta \cos \phi - 1 \right) \frac{\partial f}{\partial \varepsilon}, \tag{C21}$$

and with the use of Eq. (C18), becomes

$$\frac{\partial^2 f}{\partial \varepsilon^2} = -\frac{\sqrt{\varepsilon_0} \cos \theta \cos \phi}{2k_{\rm B} T_{\rm in} \varepsilon^{3/2}} f + \frac{1}{k_{\rm B}^2 T_{\rm in}^2} \left(\sqrt{\frac{\varepsilon_0}{\varepsilon}} \cos \theta \cos \phi - 1 \right)^2 f. \tag{C22}$$

The second-order derivative of f with respect to elevation angle is

$$\frac{\partial^2 f}{\partial \theta^2} = -\frac{2\sqrt{\varepsilon\varepsilon_0}\cos\theta\cos\phi}{k_{\rm B}T_{\rm in}} f - \frac{2\sqrt{\varepsilon\varepsilon_0}\sin\theta\cos\phi}{k_{\rm B}T_{\rm in}} \frac{\partial f}{\partial \theta}, \quad (C23)$$

and with the use of Eq. (C19), becomes

$$\frac{\partial^2 f}{\partial \theta^2} = -\frac{2\sqrt{\varepsilon\varepsilon_0}\cos\theta\cos\phi}{k_{\rm B}T_{\rm in}}f + \frac{4\varepsilon\varepsilon_0\sin^2\theta\cos^2\phi}{k_{\rm B}^2T_{\rm in}^2}f. \tag{C24}$$

Finally, the second-order derivative of f with respect to the azimuth angle is

$$\frac{\partial^2 f}{\partial \phi^2} = -\frac{2\sqrt{\varepsilon\varepsilon_0}\cos\theta\cos\phi}{k_{\rm B}T_{\rm in}} f - \frac{2\sqrt{\varepsilon\varepsilon_0}\cos\theta\sin\phi}{k_{\rm B}T_{\rm in}} \frac{\partial f}{\partial \phi}, \quad (C25)$$

and with the use of Eq. (C20), becomes

$$\frac{\partial^2 f}{\partial \phi^2} = -\frac{2\sqrt{\varepsilon\varepsilon_0}\cos\theta\cos\phi}{k_{\rm B}T_{\rm in}} f + \frac{4\varepsilon\varepsilon_0\cos^2\theta\sin^2\phi}{k_{\rm B}^2T_{\rm in}^2} f. \tag{C26}$$

We now evaluate Eq. (C16), using the above-mentioned expressions for the second-order plasma derivatives. Figure 9 shows 1D cuts of the individual terms of δf at $\varepsilon = \varepsilon_0$ and $\phi = 0^\circ$, calculated for our concept instrument acceptance widths and a Maxwellian f with density $N_{\rm in} = 10~{\rm cm}^{-3}$, bulk energy $\varepsilon_0 = 1.9~{\rm keV}$ (velocity along $\theta = \phi = 0^\circ$), and temperature $k_{\rm B}T_{\rm in} = 60~{\rm eV}$. The first term, which describes the error due to the unresolved changes of f over ε within each bin, is the smallest. The second and third terms are the dominant terms, indicating that the unresolved changes of f over elevation and azimuth within the instrument bins contribute the most to the errors we investigate in this study.

We also examine the behavior of δf for different input speeds (bulk energies) and temperatures. Figure 10(a) shows 1D cuts of δf at the bulk energy $(\varepsilon = \varepsilon_0)$ and azimuth $\phi = 0^\circ$, for four Maxwellian distributions with the same density, $N_{\rm in} = 10 \text{ cm}^{-3}$, and the same bulk energy, $\varepsilon_0 = 1.9 \text{ keV}$, but different input temperatures. The blue curve is the calculation for $k_B T_{in} = 50$ eV, the cyan curve for $k_B T_{in} = 55$ eV, the orange curve for $k_B T_{in} = 60$ eV, and the red curve for $k_B T_{in} = 65$ eV. Figure 10(b) shows the same cuts for four Maxwellian distributions with the same density, $N_{\rm in} = 10 \text{ cm}^{-3}$, and same temperature, $k_{\rm B}T_{\rm in}$ = 60 eV, but different bulk energies. The red curve is for ε_0 = 1700 eV, the orange curve is for ε_0 = 1900 eV, the cyan curve for ε_0 = 2100 eV, and the blue curve for ε_0 = 2300 eV. We see that δf is always negative at the core, and its minimum value decreases with increasing speed and/or decreasing temperature. For colder and/or faster protons, δf becomes positive for smaller absolute θ values and exhibits local maxima that are greater than

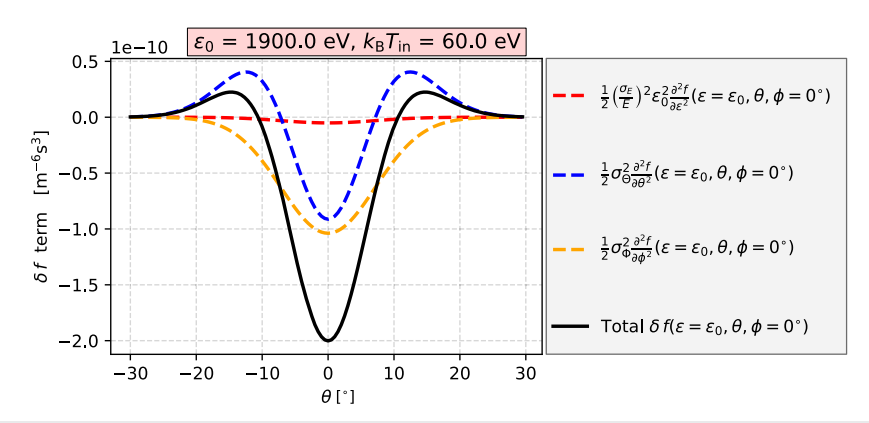


FIG. 9. 1D cuts of the parameter δf (black) and its individual terms (red, blue and orange) at the bulk energy ($\varepsilon = \varepsilon_0$) and azimuth $\phi = 0^\circ$, considering Maxwellian plasma with $N_{\rm in} = 10~{\rm cm}^{-3}$, $\varepsilon_0 = 1900~{\rm eV}$ and $k_{\rm B}T_{\rm in} = 60~{\rm eV}$. The red curve indicates the 1D cut of the first term of δf , which has the second-order derivative of f with respect to energy. The blue curve indicates the 1D cut of the second term, which has the second-order derivative of f with respect to elevation, and the orange curve is the 1D cut of the third term, which has the second-order derivative of f with respect to azimuth.

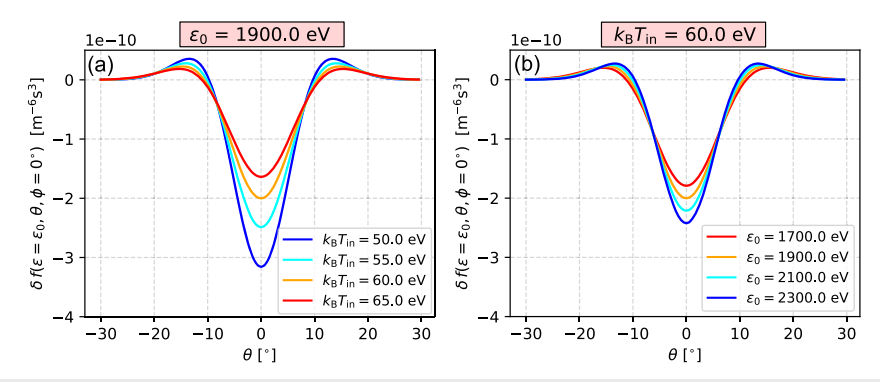


FIG. 10. δf function and its dependence on the plasma bulk energy and temperature. (a) 1D cuts of δf at the bulk energy ($\varepsilon = \varepsilon_0$) and azimuth $\phi = 0^\circ$, for four Maxwellian distributions with the same bulk energy $\varepsilon_0 = 1.9$ keV, but different input temperatures; $k_B T_{in} = 50$ eV (blue), $k_B T_{in} = 55$ eV (cyan), $k_B T_{in} = 60$ eV (orange), and $k_B T_{in} = 65$ eV (red). (b) 1D cuts of δf at the bulk energy ($\varepsilon = \varepsilon_0$) and azimuth $\phi = 0^\circ$, for four Maxwellian distributions with the same temperature $k_B T_{in} = 60$ eV, but different bulk energies; $\varepsilon_0 = 1700$ eV (red), $\varepsilon_0 = 1900$ eV (orange), $\varepsilon_0 = 2100$ eV (cyan), and $\varepsilon_0 = 2300$ eV(blue). All distributions have the same density, $N_{in} = 10$ cm⁻³.

 δf functions for slower and/or hotter protons. Although the derivatives of f vary within individual bins, for the certain example we show in Fig. 7, $\delta f(E,\Theta,\Phi)$ evaluated at the center of the bins captures the uncertainties accurately. However, for colder and faster distributions, we recommend evaluating higher-order derivatives of f as well, in order to capture the uncertainties with the analytical expression accurately.

REFERENCES

¹D. T. Young, J. J. Berthelier, M. Blanc, J. L. Burch, A. J. Coates, R. Goldstein, M. Grande, T. W. Hill, R. E. Johnson, V. Kelha, D. J. Mccomas, E. C. Sittler, K. R. Svenes, K. Szegö, P. Tanskanen, K. Ahola, D. Anderson, S. Bakshi, R. A. Baragiola, B. L. Barraclough, R. K. Black, S. Bolton, T. Booker, R. Bowman, P. Casey, F. J. Crary, D. Delapp, G. Dirks, N. Eaker, H. Funsten, J. D. Furman, J. T. Gosling, H. Hannula, C. Holmlund, H. Huomo, J. M. Illiano, P. Jensen, M. A. Johnson, D. R. Linder, T. Luntama, S. Maurice, K. P. Mccabe, K. Mursula, B. T. Narheim, J. E. Nordholt, A. Preece, J. Rudzki, A. Ruitberg, K. Smith, S. Szalai, M. F. Thomsen, K. Viherkanto, J. Vilppola, T. Vollmer, T. E. Wahl, M. Wüest, T. Ylikorpi, and C. Zinsmeyer, Space Sci. Rev. 114, 1 (2004).

²S. Barabash, R. Lundin, H. Andersson, K. Brinkfeldt, A. Grigoriev, H. Gunell, M. Holmström, M. Yamauchi, K. Asamura, P. Bochsler, P. Wurz, R. Cerulli-Irelli, A. Mura, A. Milillo, M. Maggi, S. Orsini, A. J. Coates, D. R. Linder, D. O. Kataria, C. C. Curtis, K. C. Hsieh, B. R. Sandel, R. A. Frahm, J. R. Sharber, J. D. Winningham, M. Grande, E. Kallio, H. Koskinen, P. Riihelä, W. Schmidt, T. Säles, J. U. Kozyra, N. Krupp, J. Woch, S. Livi, J. G. Luhmann, S. McKenna-Lawlor, E. C. Roelof, D. J. Williams, J.-A. Sauvaud, A. Fedorov, and J.-J. Thocaven, Space Sci. Rev. 126, 113 (2006).

³ H. Nilsson, R. Lundin, K. Lundin, S. Barabash, H. Borg, O. Norberg, A. Fedorov, J.-A. Sauvaud, H. Koskinen, E. Kallio, P. Riihelä, and J. L. Burch, Space Sci. Rev. 128, 671 (2007).

⁴C. Pollock, T. Moore, A. Jacques, J. Burch, U. Gliese, Y. Saito, T. Omoto, L. Avanov, A. Barrie, V. Coffey, J. Dorelli, D. Gershman, B. Giles, T. Rosnack, C. Salo, S. Yokota, M. Adrian, C. Aoustin, C. Auletti, S. Aung, V. Bigio, N. Cao, M. Chandler, D. Chornay, K. Christian, G. Clark, G. Collinson, T. Corris, A. De Los Santos, R. Devlin, T. Diaz, T. Dickerson, C. Dickson, A. Diekmann, F. Diggs, C. Duncan, A. Figueroa-Vinas, C. Firman, M. Freeman, N. Galassi, K. Garcia, G. Goodhart, D. Guererro, J. Hageman, J. Hanley, E. Hemminger, M. Holland, M. Hutchins, T. James, W. Jones, S. Kreisler, J. Kujawski, V. Lavu, J. Lobell, E. LeCompte, A. Lukemire, E. MacDonald, A. Mariano, T. Mukai, K. Narayanan, Q. Nguyan, M. Onizuka, W. Paterson, S. Persyn, B. Piepgrass, F. Cheney, A. Rager, T. Raghuram, A. Ramil, L. Reichenthal, H. Rodriguez, J. Rouzaud, A. Rucker, Y. Saito,

- M. Samara, J.-A. Sauvaud, D. Schuster, M. Shappirio, K. Shelton, D. Sher, D. Smith, K. Smith, S. Smith, D. Steinfeld, R. Szymkiewicz, K. Tanimoto, J. Taylor, C. Tucker, K. Tull, A. Uhl, J. Vloet, P. Walpole, S. Weidner, D. White, G. Winkert, P.-S. Yeh, and M. Zeuch, Space Sci. Rev. 199, 331 (2016).
- ⁵D. J. McComas, N. Alexander, F. Allegrini, F. Bagenal, C. Beebe, G. Clark, F. Crary, M. I. Desai, A. De Los Santos, D. Demkee, J. Dickinson, D. Everett, T. Finley, A. Gribanova, R. Hill, J. Johnson, C. Kofoed, C. Loeffler, P. Louarn, M. Maple, W. Mills, C. Pollock, M. Reno, B. Rodriguez, J. Rouzaud, D. Santos-Costa, P. Valek, S. Weidner, P. Wilson, R. J. Wilson, and D. White, Space Sci. Rev. 213, 547 (2017).
- ⁶R. Livi, D. E. Larson, J. C. Kasper, R. Abiad, A. W. Case, K. G. Klein, D. W. Curtis, G. Dalton, M. Stevens, K. E. Korreck, G. Ho, M. Robinson, C. Tiu, P. L. Whittlesey, J. L. Verniero, J. Halekas, J. McFadden, M. Marckwordt, A. Slagle, M. Abatcha, A. Rahmati, and M. D. McManus, Astrophys. J. 938, 138 (2022).
- ⁷C. J. Owen, R. Bruno, S. Livi, P. Louarn, K. Al Janabi, F. Allegrini, C. Amoros, R. Baruah, A. Barthe, M. Berthomier, S. Bordon, C. Brockley-Blatt, C. Brysbaert, G. Capuano, M. Collier, R. DeMarco, A. Fedorov, J. Ford, V. Fortunato, I. Fratter, A. B. Galvin, B. Hancock, D. Heirtzler, D. Kataria, L. Kistler, S. T. Lepri, G. Lewis, C. Loeffler, W. Marty, R. Mathon, A. Mayall, G. Mele, K. Ogasawara, M. Orlandi, A. Pacros, E. Penou, S. Persyn, M. Petiot, M. Phillips, L. Přech, J. M. Raines, M. Reden, A. P. Rouillard, A. Rousseau, J. Rubiella, H. Seran, A. Spencer, J. W. Thomas, J. Trevino, D. Verscharen, P. Wurz, A. Alapide, L. Amoruso, N. André, C. Anekallu, V. Arciuli, K. L. Arnett, R. Ascolese, C. Bancroft, P. Bland, M. Brysch, R. Calvanese, M. Castronuovo, I. Čermák, D. Chornay, S. Clemens, J. Coker, G. Collinson, R. D'Amicis, I. Dandouras, R. Darnley, D. Davies, G. Davison, A. De Los Santos, P. Devoto, G. Dirks, E. Edlund, A. Fazakerley, M. Ferris, C. Frost, G. Fruit, C. Garat, V. Génot, W. Gibson, J. A. Gilbert, V. de Giosa, S. Gradone, M. Hailey, T. S. Horbury, T. Hunt, C. Jacquey, M. Johnson, B. Lavraud, A. Lawrenson, F. Leblanc, W. Lockhart, M. Maksimovic, A. Malpus, F. Marcucci, C. Mazelle, F. Monti, S. Myers, T. Nguyen, J. Rodriguez-Pacheco, I. Phillips, M. Popecki, K. Rees, S. A. Rogacki, K. Ruane, D. Rust, M. Salatti, J. A. Sauvaud, M. O. Stakhiv, J. Stange, T. Stubbs, T. Taylor, J.-D. Techer, G. Terrier, R. Thibodeaux, C. Urdiales, A. Varsani, A. P. Walsh, G. Watson, P. Wheeler, G. Willis, R. F. Wimmer-Schweingruber, B. Winter, J. Yardley, and I. Zouganelis, Astron. Astrophys. 642, A16 (2020).
- ⁸P. Bevington and D. Robinson, *Data Reduction and Error Analysis for the Physical Sciences* (McGraw-Hill, 1992), Vol. 1.
- ⁹R. J. Wilson, Earth Space Sci. 2, 201 (2015).
- ¹⁰G. Nicolaou, D. J. McComas, F. Bagenal, and H. A. Elliott, J. Geophys. Res.: Space Phys. 119, 3463, https://doi.org/10.1002/2013JA019665 (2014).
- ¹¹ M. R. Stoneking and D. J. Den Hartog, Rev. Sci. Instrum. **68**, 914 (1997).
- ¹²G. Nicolaou, R. Wicks, G. Livadiotis, D. Verscharen, C. Owen, and D. Kataria, Entropy 22, 103 (2020).
- ¹³ G. Nicolaou, G. Livadiotis, N. Sarlis, and C. Ioannou, RAS Tech. Instrum. 3, 874 (2024).
- ¹⁴G. Nicolaou, G. Livadiotis, and C. Ioannou, Astrophys. J. 977, 168 (2024).
- ¹⁵G. Nicolaou, Astrophys. Space Sci. 368, 3 (2023).
- ¹⁶Z. Wang, B. Miao, Y. Wang, C. Shen, L. Kong, W. Li, B. Tang, J. Ma, F. Qiao, L. Wang, A. Zhang, and L. Li, Adv. Space Res. 74, 5282 (2024).
- ¹⁷G. Nicolaou, F. Allegrini, G. Livadiotis, and R. W. Ebert, Rev. Sci. Instrum. 93, 103305 (2022).
- ¹⁸T. K. Kim, R. W. Ebert, P. W. Valek, F. Allegrini, D. J. McComas, F. Bagenal, J. E. P. Connerney, G. Livadiotis, M. F. Thomsen, R. J. Wilson,

- and S. J. Bolton, J. Geophys. Res.: Space Phys. 125, e2019JA027696 (2020), https://doi.org/10.1029/2019JA027696.
- ¹⁹P.-Y. Parent, D. Verscharen, G. Nicolaou, and C. J. Owen, "RAS Tech. Instrum. 3, 844 (2024).
- ²⁰D. Verscharen and E. Marsch, Ann. Geophys. 29, 909 (2011).
- ²¹G. Nicolaou, D. Verscharen, R. T. Wicks, and C. J. Owen, Astrophys. J. 886, 101 (2019).
- ²²G. Nicolaou, G. Livadiotis, C. J. Owen, D. Verscharen, and R. T. Wicks, Astrophys. J. 864, 3 (2018).
- $^{\bf 23}$ H. Zhang, D. Verscharen, and G. Nicolaou, Space Weather $\bf 22$, e2023SW003671, https://doi.org/10.1029/2023SW003671 (2024).
- ²⁴O. W. Roberts, R. Nakamura, V. N. Coffey, D. J. Gershman, M. Volwerk, A. Varsani, B. L. Giles, J. C. Dorelli, and C. Pollock, J. Geophys. Res.: Space Phys. 126, e2021JA029784, https://doi.org/10.1029/2021JA029784 (2021).
- ²⁵ L. B. Wilson, K. A. Goodrich, D. L. Turner, I. J. Cohen, P. L. Whittlesey, and S. J. Schwartz, Front. Astron. Space Sci. 9, 1063841 (2022).
- ²⁶H. A. Elliott, D. J. McComas, P. Valek, G. Nicolaou, S. Weidner, and G. Livadiotis, Astrophys. J., Suppl. Ser. **223**, 19 (2016).
- ²⁷G. Nicolaou and G. Livadiotis, Astrophys. Space Sci. **361**, 359 (2016).
- ²⁸B. Lavraud and D. E. Larson, J. Geophys. Res.: Space Phys. **121**, 8462, https://doi.org/10.1002/2016JA022591 (2016).
- ²⁹D. McComas, F. Allegrini, F. Bagenal, P. Casey, P. Delamere, D. Demkee, G. Dunn, H. Elliott, J. Hanley, K. Johnson, J. Langle, G. Miller, S. Pope, M. Reno, B. Rodriguez, N. Schwadron, P. Valek, and S. Weidner, Space Sci. Rev. 140, 261 (2008).
- ³⁰G. Nicolaou, R. P. Haythornthwaite, and A. J. Coates, Front. Astron. Space Sci. 9, 861433 (2022).
- ³¹G. Nicolaou, R. T. Wicks, I. J. Rae, and D. O. Kataria, Space Weather 18, e2020SW002559, https://doi.org/10.1029/2020SW002559 (2020).
- ³²G. Nicolaou, G. Livadiotis, and R. T. Wicks, Entropy 22, 212 (2020).
- ³³G. R. Lewis, N. André, C. S. Arridge, A. J. Coates, L. K. Gilbert, D. R. Linder, and A. M. Rymer, Planet. Space Sci. 56, 901 (2008).
- ³⁴J. W. Freeman, Geophys. Res. Lett. **15**, 88, https://doi.org/10.1029/ GL015i001p00088 (1988).
- ³⁵G. Nicolaou and G. Livadiotis, Entropy 22, 541 (2020).
- ³⁶D. Stansby, D. Perrone, L. Matteini, T. S. Horbury, and C. S. Salem, Astron. Astrophys. **623**, L2 (2019).
- ³⁷R. Bruno, R. De Marco, R. D'Amicis, D. Perrone, M. F. Marcucci, D. Telloni, R. Marino, L. Sorriso-Valvo, V. Fortunato, G. Mele, F. Monti, A. Fedorov, P. Louarn, C. J. Owen, and S. Livi, Astrophys. J. 969, 106 (2024).
- ³⁸ H. DeWeese, B. A. Maruca, R. A. Qudsi, A. Chasapis, M. Pultrone, E. Johnson, S. K. Vines, M. A. Shay, W. H. Matthaeus, R. G. Gomez, S. A. Fuselier, B. L. Giles, D. J. Gershman, C. T. Russell, R. J. Strangeway, J. L. Burch, and R. B. Torbert, Astrophys. J. **941**, 12 (2022).
- ³⁹ D. Vech, M. L. Stevens, K. W. Paulson, D. M. Malaspina, A. W. Case, K. G. Klein, and J. C. Kasper, Astrophys. 650, A198 (2021).
- ⁴⁰R. J. Wilson, R. L. Tokar, M. G. Henderson, T. W. Hill, M. F. Thomsen, and D. H. Pontius, Jr., J. Geophys. Res.: Space Phys. 113, https://doi.org/10.1029/2008JA013486 (2008).
- ⁴¹ E. Marsch, Space Sci. Rev. **172**, 23 (2012).
- ⁴²G. Livadiotis and D. J. McComas, Space Sci. Rev. **175**, 183 (2013).
- ⁴³D. Verscharen, K. G. Klein, and B. A. Maruca, Living Rev. Sol. Phys. 16, 5 (2019).